The Astrophysical Journal, 893:75 (16pp), 2020 April 10 https://doi.org/10.3847/1538-4357/ab8066

Generation of Solenoidal Modes and Magnetic Fields in Turbulence Driven by Compressive Driving

Jeonghoon Lim[1], Jungyeon Cho[1,2], and Heesun Yoon[2,1]
[1] Department of Astronomy and Space Science, Chungnam National University, 99, Daehak-ro, Yuseong-gu, Daejeon, 34134, Republic of Korea
jhLim0918@o.cnu.ac.kr, jcho@cnu.ac.kr, hsyoon@kasi.re.kr
[2] Korea Astronomy and Space Science Institute, 776, Daedeokdae-ro, Yuseong-gu, Daejeon, 34055, Republic of Korea
Received 2020 January 14; revised 2020 February 28; accepted 2020 March 15; published 2020 April 16

Abstract

We perform numerical simulations of hydrodynamic (HD) and magnetohydrodynamic (MHD) turbulence driven by compressive driving, to study the generation of solenoidal velocity components and the small-scale magnetic field. We mainly focus on the effects of mean magnetic field (B_0) and the sonic Mach number (M_s). The dependence of solenoidal ratio (i.e., ratio of solenoidal to kinetic energies) and magnetic energy density on M_s in compressively driven turbulence is already established, but that on B_0 is not yet. We also consider two different driving schemes in terms of the correlation timescale of forcing vectors: a finite-correlated driving and a delta-correlated driving. Our findings are as follows. First, when we fix the value of B_0, the solenoidal ratio after saturation increases as M_s increases. A similar trend is observed for generation of magnetic field when B_0 is small. Second, when we fix the value of M_s, HD and MHD simulations result in similar solenoidal ratios when B_0 is not strong (say, $M_A \gtrsim 5$, where M_A is Alfvén Mach number). However, the ratio increases when $M_A \lesssim 5$. Roughly speaking, the magnetic energy density after saturation is a linearly increasing function of B_0 irrespective of M_s. Third, generation of the solenoidal velocity component is not sensitive to numerical resolution, but that of magnetic energy density is mildly sensitive. Finally, when initial conditions are same, the finite-correlated driving always produces more solenoidal velocity and small-scale magnetic field components than the delta-correlated driving. We additionally analyze the vorticity equation to understand why higher M_s and B_0 yield a larger quantity of the solenoidal velocity component.

Unified Astronomy Thesaurus concepts: Magnetohydrodynamics (1964); Interplanetary turbulence (830); Interstellar medium (847); Interstellar magnetic fields (845); Magnetohydrodynamical simulations (1966); Intracluster medium (858)

1. Introduction

Turbulence is ubiquitous in almost all astrophysical media, ranging from the interstellar medium (ISM) (e.g., Larson 1981; Elmegreen & Scalo 2004; Mac Low & Klessen 2004; McKee & Ostriker 2007) to the intracluster medium (ICM) (e.g., Kulsrud et al. 1997; Schuecker et al. 2004; Ryu et al. 2008; Hitomi Collaboration et al. 2016; Vazza et al. 2017). Turbulence in cold (10 K) and dense interstellar molecular clouds has Mach numbers (M_s) of $\sim$ a few or even larger than 10 (see, e.g., Larson 1981). Such supersonic turbulence plays essential roles in star formation processes in the ISM (see Mac Low & Klessen 2004 for a review). Unlike this, ICM turbulence is usually subsonic, with $M_s \lesssim 1/2$ (see, e.g., Ryu et al. 2008; Brunetti & Jones 2014). It also has crucial impacts on astrophysical phenomena in the ICM, including amplification of weak seed magnetic fields (e.g., Schekochihin et al. 2004; Ryu et al. 2008; Cho 2014; Federrath 2016).

Magnetic fields permeated in turbulence appear in a variety of astrophysical objects and have huge impacts on them. For instance, they significantly affect the evolution of molecular clouds and the fragmentation process of cores in the ISM; for a review, see Hennebelle & Inutsuka (2019) and Krumholz & Federrath (2019). Moreover, magnetic fields and turbulence in the ICM can accelerate cosmic-ray electrons and protons (see Brunetti & Jones 2014 and references therein).

The strength of magnetic fields varies from the ISM to the ICM. Observations of dust polarization in interstellar molecular cloud cores suggest that the strength is typically $\sim$mG (see Crutcher 2012 and references therein). On the other hand, observations of synchrotron emission from galaxy clusters and Faraday rotation reveal that magnetic fields on the order of μG exist in the ICM (see, e.g., Carilli & Taylor 2002; Govoni & Feretti 2004; Ryu et al. 2012).

Turbulence in astrophysical media has a mixture of both solenoidal ($\nabla \cdot \boldsymbol{v} = 0$) and compressive ($\nabla \times \boldsymbol{v} = 0$) velocity components, where $\boldsymbol{v}$ is velocity. Similarly, the turbulence driving force ($\boldsymbol{f}$) can also have solenoidal ($\nabla \cdot \boldsymbol{f} = 0$) and compressive ($\nabla \times \boldsymbol{f} = 0$) components. In turbulence studies, solenoidal driving has been predominantly used. However, there also have been multiple works that made use of compressive driving. Earlier studies have shown that the driving mechanism affects characteristics of turbulence or related physical phenomena. For example, compressively driven turbulence has a wider probability density function (PDF) of density (Federrath et al. 2008, 2010), produces more intermittent structures (Federrath et al. 2009; Yoon & Cho 2019), and yields much more efficient star formation rates (Federrath & Klessen 2012) than solenoidally driven turbulence.

When solenoidal driving forces turbulence, it is evident that solenoidal energy dominates over compressive. This is independent of both its Mach number (see, e.g., Bertoglio et al. 2001; Federrath et al. 2011) and its degree of magnetization; for hydrodynamic turbulence, see Kritsuk et al. (2007), Federrath et al. (2010), and Federrath (2013), and for magnetohydrodynamic turbulence, see Boldyrev et al. (2002), Cho & Lazarian (2003),

Kritsuk et al. (2010), Federrath et al. (2011), and Porter et al. (2015).

When compressive driving forces turbulence, previous numerical studies have shown that the solenoidal velocity component in such turbulence can be generated at shocks and amplified by vortex stretching (Federrath et al. 2011; Porter et al. 2015). In particular, Federrath et al. (2011) found that solenoidal energy accounts for up to ∼40% of total kinetic energy when turbulence is supersonic and a weak mean magnetic field is present. However, since they considered only a single mean magnetic field strength, the dependence of the solenoidal ratio (i.e., the ratio of solenoidal to total kinetic energies) on the mean magnetic field strength in compressively driven turbulence is not yet fully determined. In this regard, we mainly aim at determining the solenoidal ratio in compressively driven turbulence by taking various strengths of the mean magnetic field into account. We also investigate the role of the magnetic fields in the generation of solenoidal modes.

Amplification of magnetic field on scales comparable to or smaller than the driving scale by turbulent motions is known as the small-scale turbulence dynamo. In this process, turbulent motions stretch, twist, and fold magnetic field lines, which in turn results in conversion of kinetic energy of turbulence to magnetic energy (see, e.g., Batchelor 1950; Cho & Vishniac 2000; Haugen et al. 2004; Schekochihin et al. 2004, 2007; Brandenburg & Subramanian 2005; Cho et al. 2009; Federrath 2016 for details; see also Appendix in Cho 2014). Since the dynamo action is mainly achieved by solenoidal motions of turbulence, it is apparent that the types of driving have an influence on the process. For solenoidal driving, comprehensive studies exist related to the turbulence dynamo. Those studies have numerically shown that solenoidal driving efficiently amplifies small-scale magnetic field via field line stretching, and the resulting magnetic energy becomes comparable to kinetic energy at saturation (Cho & Vishniac 2000; Haugen et al. 2003; Schekochihin et al. 2004, 2007; Ryu et al. 2008; Cho et al. 2009; Federrath et al. 2011; Cho & Yoo 2012; Porter et al. 2015). On the other hand, compressive driving cannot efficiently excite a small-scale magnetic field because it does not produce a great enough solenoidal velocity component to amplify the magnetic field. As a result, the amplified magnetic field after turbulence reaches the saturation stage is dynamically insignificant (Federrath et al. 2011; Porter et al. 2015). Apart from its inefficiency, earlier studies have revealed relatively fewer facts regarding the turbulence dynamo in compressively driven turbulence. In this paper, we provide a more comprehensive study on this topic. To be specific, we consider a wide range of the mean magnetic field strengths and try to estimate an upper limit on the magnetic saturation level in compressively driven turbulence when numerical resolution is very high and the mean magnetic field is very weak.

The paper is organized as follows. We explain our numerical method in Section 2. We present results related to generation of solenoidal modes and small-scale magnetic fields in Sections 3 and 4, respectively. We discuss our findings in Sections 5 and 6, and give a summary in Section 7.

2. Numerical Method

2.1. Numerical Code

We use an essentially non-oscillatory scheme (see Cho & Lazarian 2002) to solve the ideal magnetohydrodynamic (MHD) equations in a periodic box of size 2π:

$$\frac{\partial \rho}{\partial t} + \nabla \cdot (\rho \boldsymbol{v}) = 0, \tag{1}$$

$$\rho\left(\frac{\partial \boldsymbol{v}}{\partial t} + \boldsymbol{v} \cdot \nabla \boldsymbol{v}\right) + c_s^2 \nabla \rho - (\nabla \times \boldsymbol{B}) \times \boldsymbol{B} = \rho \boldsymbol{f}, \tag{2}$$

$$\frac{\partial \boldsymbol{B}}{\partial t} - \nabla \times (\boldsymbol{v} \times \boldsymbol{B}) = 0, \tag{3}$$

$$\nabla \cdot \boldsymbol{B} = 0, \tag{4}$$

with an isothermal equation of state $p = c_s^2 \rho$, where c_s is the sound speed, ρ is the density, p is the gas pressure, $\boldsymbol{f}$ is a driving force (see Section 2.2 for details), $\boldsymbol{v}$ is the velocity, and $\boldsymbol{B}$ is the magnetic field divided by $\sqrt{4\pi}$. For hydrodynamic (HD) simulations, we only solve Equations (1) and (2) with $\boldsymbol{B} = 0$. The magnetic field consists of two components: a uniform mean field ($\boldsymbol{B}_0$) and a fluctuating random field ($\boldsymbol{b}$), so that $\boldsymbol{B} = \boldsymbol{B}_0 + \boldsymbol{b}$. At $t = 0$, the density and velocity are set to one and zero, respectively, to assume a static medium with a constant density. In cases of MHD, only a mean magnetic field exists at the beginning.

2.2. Forcing Schemes

In our simulations, we drive turbulence in Fourier space using either solenoidal ($\nabla \cdot \boldsymbol{f} = 0$) or compressive ($\nabla \times \boldsymbol{f} = 0$) driving. We consider two different types of driving in terms of different correlation timescales of forcing vectors: a finite-correlated driving and a delta-correlated driving. In the former, forcing vectors continuously change with a correlation timescale comparable to the large-eddy turnover time (see Cho & Ryu 2009; see also Federrath et al. 2010). In the latter, both the direction and amplitude of driving change on a very short timescale $\Delta t = 0.001$ in code units, which roughly corresponds to a few thousandths of the large-eddy turnover time; for details, see Yoon et al. (2016). In summary, we consider the following forcing schemes:

1. Finite-correlated compressive driving.
2. Finite-correlated solenoidal driving.
3. Delta-correlated compressive driving.
4. Delta-correlated solenoidal driving.

2.3. Simulations

We use up to 1024^3 grid points in our periodic computational box. In all simulations, energy injection peaks at $k \approx 2.5$, where k is the wavenumber; see Cho & Ryu (2009) for details about the forcing wavenumbers. The strength of the mean magnetic field (B_0) ranges from 0.001 to 1.0 in MHD turbulence simulations, which is actually the Alfvén speed of the mean magnetic field (i.e., $V_A \equiv B_0/\sqrt{4\pi\rho_0}$, where ρ_0 is equal to one and 4π does not appear in our units). In our simulations, the rms velocity ($v_{\rm rms}$) is roughly one when turbulence is fully developed. Therefore, the Alfvén Mach number ($M_A \equiv v_{\rm rms}/v_A$) can be regarded as B_0^{-1} in our simulations. We change the isothermal sound speed c_s to control the sonic Mach number $M_s \equiv v_{\rm rms}/c_s$. The resulting sonic Mach number ranges from ∼0.5 to ∼10. When we present time evolutions of physical quantities, we use a normalized time: $t = t_{\rm code}/t_{\rm ed}$. Here, $t_{\rm code}$ is time in code units, and $t_{\rm ed} = L_f/v_{\rm rms}$ is large-eddy turnover time. The driving scale of turbulence L_f is about 2.5 times smaller than the computational box.

Table 1
Results of Simulations

Run	Driving	Resolution	M_s[a]	M_A ($\sim B_0^{-1}$)[b]	v_{sol}^2/v_{tot}^2[c]	b^2/v_{tot}^2[d]	(t_1, t_2)[e]
F1024MS1-$B_0$0.1	Finite-correlated compressive	1024^3	∼1	10.0	0.262	0.194	(3, 5.5)
F512MS0.5-$B_0$0.05		512^3	∼0.5	20.0	0.099	0.059	(5, 10)
F512MS0.5-$B_0$0.1		512^3	∼0.5	10.0	0.099	0.091	(5, 10)
F512MS1-$B_0$0.001		512^3	∼1	1000.0	0.249	0.033	(40, 70)
F512MS1-$B_0$0.01		512^3	∼1	100.0	0.246	0.044	(20, 30)
F512MS1-$B_0$0.05		512^3	∼1	20.0	0.280	0.091	(3, 5.5)
F512MS1-$B_0$0.1		512^3	∼1	10.0	0.275	0.162	(3, 5.5)
F512MS1-$B_0$0.2		512^3	∼1	5.0	0.307	0.250	(3, 5.5)
F512MS1-$B_0$0.6		512^3	∼1	1.7	0.491	0.441	(3, 5.5)
F512MS1-$B_0$1		512^3	∼1	1.0	0.654	0.526	(3, 6)
F512MS1-Hydro		512^3	∼1	⋯	0.317	⋯	(3, 6)
F256MS0.5-$B_0$0.001		256^3	∼0.5	1000.0	0.147	0.004	(140, 180)
F256MS0.5-$B_0$0.01		256^3	∼0.5	100.0	0.130	0.011	(30, 75)
F256MS0.5-$B_0$0.05		256^3	∼0.5	20.0	0.096	0.042	(8, 12)
F256MS0.5-$B_0$0.1		256^3	∼0.5	10.0	0.093	0.072	(8, 12)
F256MS0.5-$B_0$0.2		256^3	∼0.5	5.0	0.101	0.102	(8, 12)
F256MS0.5-$B_0$1		256^3	∼0.5	1.0	0.447	0.475	(3, 10)
F256MS1-$B_0$0.001		256^3	∼1	1000.0	0.245	0.015	(80, 160)
F256MS1-$B_0$0.01		256^3	∼1	100.0	0.237	0.026	(30, 160)
F256MS1-$B_0$0.05		256^3	∼1	20.0	0.272	0.065	(3.5.5)
F256MS1-$B_0$0.1		256^3	∼1	10.0	0.262	0.128	(3, 5.5)
F256MS1-$B_0$0.2		256^3	∼1	5.0	0.284	0.209	(3, 5.5)
F256MS1-$B_0$0.6		256^3	∼1	1.7	0.459	0.415	(3, 5.5)
F256MS1-$B_0$1		256^3	∼1	1.0	0.615	0.504	(3, 6)
F256MS3-$B_0$0.001		256^3	∼3	1000.0	0.332	0.018	(80, 160)
F256MS3-$B_0$0.01		256^3	∼3	100.0	0.336	0.024	(30, 50)
F256MS3-$B_0$0.05		256^3	∼3	20.0	0.367	0.084	(5, 12)
F256MS3-$B_0$0.1		256^3	∼3	10.0	0.452	0.157	(5, 12)
F256MS3-$B_0$0.2		256^3	∼3	5.0	0.560	0.275	(5, 12)
F256MS3-$B_0$1		256^3	∼3	1.0	0.761	0.423	(3, 10)
F256MS10-$B_0$1		256^3	∼10	1.0	0.761	0.355	(3, 10)
F256MS0.5-Hydro		256^3	∼0.5	⋯	0.132	⋯	(3, 10)
F256MS1-Hydro		256^3	∼1	⋯	0.256	⋯	(80, 160)
F256MS3-Hydro		256^3	∼3	⋯	0.350	⋯	(3, 10)
D512MS1-$B_0$0.01	Delta-correlated compressive	512^3	∼1	100.0	0.161	0.023	(20, 30)
D512MS1-$B_0$1		512^3	∼1	1.0	0.471	0.511	(3, 6)
D256MS0.5-$B_0$0.01		256^3	∼0.5	100.0	0.063	0.006	(70, 95)
D256MS1-$B_0$0.01		256^3	∼1	100.0	0.130	0.012	(40, 100)
D256MS3-$B_0$0.01		256^3	∼3	100.0	0.259	0.018	(40, 80)
D256MS0.5-$B_0$1		256^3	∼0.5	1.0	0.309	0.376	(3, 10)
D256MS1-$B_0$1		256^3	∼1	1.0	0.417	0.467	(3, 6)
D256MS3-$B_0$1		256^3	∼3	1.0	0.590	0.384	(3, 10)
D256MS10-$B_0$1		256^3	∼10	1.0	0.641	0.306	(3, 10)
D256MS0.5-Hydro		256^3	∼0.5	⋯	0.066	⋯	(3, 10)
D256MS1-Hydro		256^3	∼1	⋯	0.165	⋯	(3, 10)
D256MS3-Hydro		256^3	∼3	⋯	0.255	⋯	(3, 10)
Sol-F256MS1-$B_0$0.001	Finite-correlated solenoidal	256^3	∼1	1000.0	0.958	0.262	(30, 80)
Sol-D256MS1-$B_0$0.001	Delta-correlated solenoidal	256^3	∼1	1000.0	0.886	0.091	(30, 80)

Notes.
[a] The sonic Mach number.
[b] The Alfvén Mach number ($M_A \equiv v_{rms}/v_A$) of the mean magnetic field. Note that the rms velocity is ∼1 in our simulations and $v_A = B_0$ in our units. Therefore, in our simulations, $M_A \sim B_0^{-1}$. See Section 2.3 for details.
[c] The solenoidal ratio after saturation. Here, $\boldsymbol{v}_{sol}$ is solenoidal velocity component and $\boldsymbol{v}_{tot}$ is total velocity.
[d] The magnetic saturation level after saturation. Here, b^2 is small-scale magnetic energy density.
[e] The time interval in the unit of large-eddy turnover time (t_{ed}) for averaging the physical quantities.

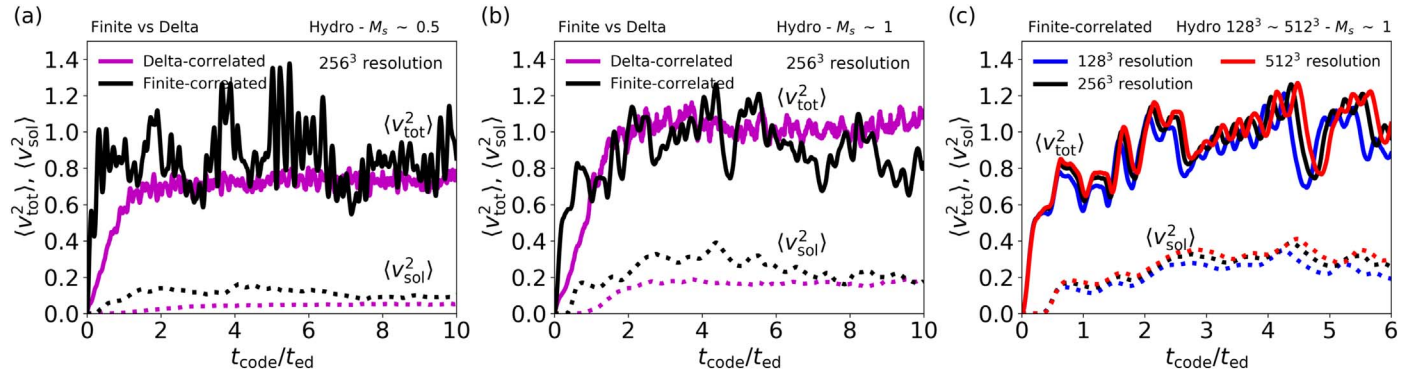

Figure 1. Time evolution of $\langle v_{tot}^2 \rangle$ (solid curves) and $\langle v_{sol}^2 \rangle$ (dotted curves) for HD turbulence driven by compressive driving, where $\langle \cdots \rangle$ denotes spatial average. (a) $M_s \sim 0.5$ and 256^3 resolution. (b) $M_s \sim 1$ and 256^3 resolution. (c) Resolution study only for the finite-correlated compressive driving and $M_s \sim 1$. Black and magenta curves in the left and the middle panels represent the finite-correlated and the delta-correlated compressive drivings, respectively. Blue, black, and red curves in the right panel correspond to 128^3, 256^3, and 512^3 resolutions, respectively.

Table 1 lists our simulations. We use the notation X_1X_2 MSX_3-B_0X_4, where $X_1 = F$ or D refers to either the finite-correlated or the delta-correlated driving[3]; $X_2 = 256$, 512, or 1024 refers to the number of grid points in each spatial direction; $X_3 = 0.5$, 1, 3, or 10 refers to the sonic Mach number; $X_4 = 0.001$, 0.01, 0.05, 0.1, 0.2, 0.6, or 1.0 refers to the strength of the mean magnetic field; and $B_0X_4 =$ Hydro refers to the HD simulation.

We use the following notations in this paper:

1. $\boldsymbol{v}_{tot}$ ($\equiv \boldsymbol{v}_{sol} + \boldsymbol{v}_{comp}$): total velocity.
2. $\boldsymbol{v}_{sol}$, $\boldsymbol{v}_{comp}$: solenoidal and compressive velocity components, respectively.
3. v_{sol}^2/v_{tot}^2 ($\equiv \langle v_{sol}^2 \rangle / \langle v_{tot}^2 \rangle$): we refer to this as *solenoidal ratio*. Here, $\langle \cdots \rangle$ denotes spatial average.
4. B ($\equiv \sqrt{B_0^2 + b^2}$): total magnetic field strength.
5. B_0: mean magnetic field strength. Note that, in our units, B_0 is actually the Alfvén speed of the mean field.
6. b ($\equiv \sqrt{\langle b^2 \rangle}$): random magnetic field strength.
7. b^2/v_{tot}^2 ($\equiv \langle b^2 \rangle / \langle v_{tot}^2 \rangle$): we refer to this as the *magnetic saturation level*.

3. Generation of Solenoidal Modes

In this section, we investigate generation of the solenoidal velocity component in compressively driven turbulence. In Section 3.1, we consider HD turbulence. We describe effects of the sonic Mach number (M_s) and the mean magnetic field (B_0) for MHD turbulence in Sections 3.2 and 3.3, respectively.

3.1. Effects of the Sonic Mach Number in HD Turbulence

Figure 1 shows the time evolution of $\langle v_{tot}^2 \rangle$ and $\langle v_{sol}^2 \rangle$ in HD turbulence driven by compressive driving. Panels (a) and (b) are for comparison of the finite-correlated compressive driving with the delta-correlated compressive driving at 256^3 resolution, which are represented as black and magenta curves, respectively. Figure 1(c) shows a resolution study for the finite-correlated compressive driving, in which blue, black, and red curves denote 128^3, 256^3, and 512^3 resolutions, respectively.

[3] We additionally consider two simulations with solenoidal driving. They are notated by Sol-D256MS1-$B_0$0.001 and Sol-F256MS1-$B_0$0.001, respectively. All other simulations, which do not start with Sol-, are for compressive driving (see Table 1).

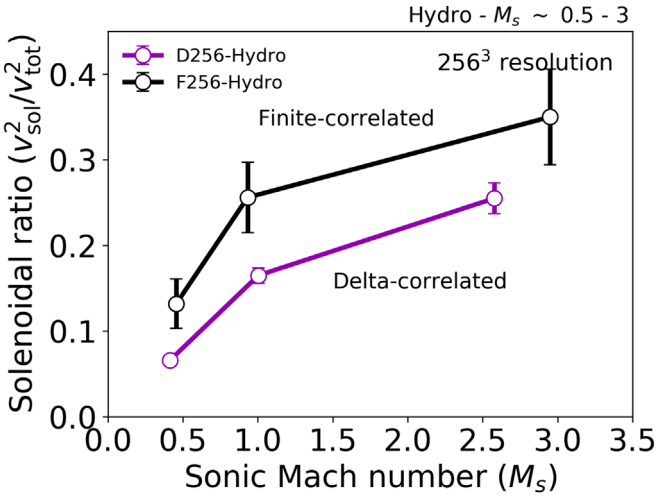

Figure 2. Average values of the solenoidal ratio (v_{sol}^2/v_{tot}^2) as a function of the sonic Mach number (M_s) for the HD simulations. Black and magenta circles indicate the finite-correlated and the delta-correlated compressive drivings for 256^3 resolution, respectively. Error bars represent standard deviations. In Table 1, the average values and the time intervals for taking an average are shown.

The sonic Mach number is ~0.5 in the left panel, and ~1 in the middle and the right panels.

As we can see from the figure, turbulence seems to saturate before approximately $3t_{ed}$, and the level of $\langle v_{sol}^2 \rangle$ at the saturation stage is much lower than that of $\langle v_{tot}^2 \rangle$ in all simulations presented. In addition, we can clearly see from Figure 1(a) and (b) that the finite-correlated compressive driving (see black curves) yields nearly the same levels of $\langle v_{tot}^2 \rangle$ regardless of M_s, but $\langle v_{sol}^2 \rangle$ for $M_s \sim 1$ is larger than that for $M_s \sim 0.5$. For the delta-correlated compressive driving (see magenta curves), the level of both $\langle v_{tot}^2 \rangle$ and $\langle v_{sol}^2 \rangle$ for $M_s \sim 1$ is larger than that for $M_s \sim 0.5$. Regarding numerical resolution effect, Figure 1(c) clearly shows that the time evolutions for three simulations with 128^3, 256^3, and 512^3 resolutions are virtually identical, which means that the generation of solenoidal modes is very insensitive to the numerical resolution.

Figure 2 shows the average values of the solenoidal ratio as a function of M_s. Black and magenta circles correspond to the finite-correlated and the delta-correlated compressive drivings,

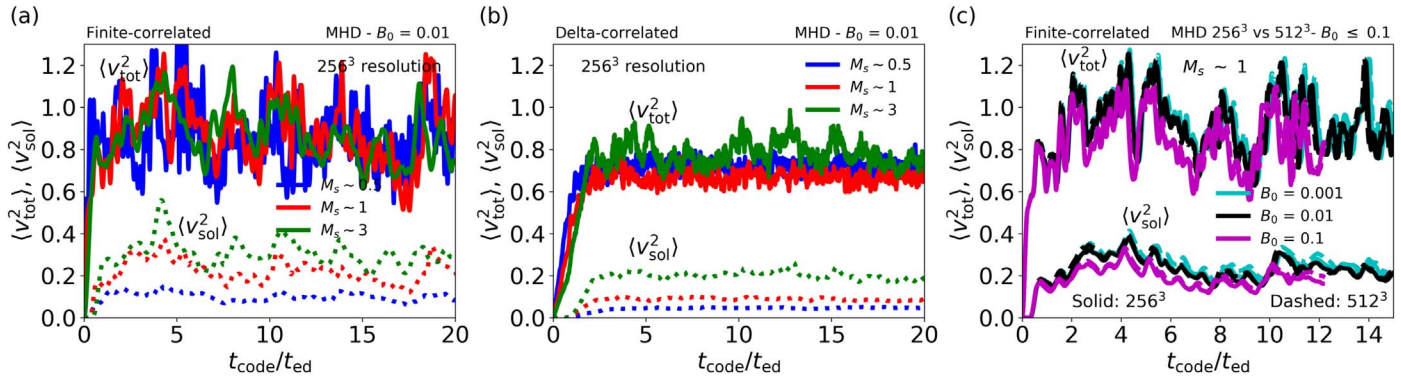

Figure 3. Time evolution of $\langle v_{tot}^2 \rangle$ and $\langle v_{sol}^2 \rangle$ for MHD turbulence simulations with $B_0 \leqslant 0.1$. (a) Finite-correlated compressive driving with $B_0 = 0.01$. (b) Delta-correlated compressive driving with $B_0 = 0.01$. (c) Resolution study for $B_0 \leqslant 0.1$ and $M_s \sim 1$. Blue, red, and green solid (dotted) curves in the left and the middle panels represent $\langle v_{tot}^2 \rangle$ ($\langle v_{sol}^2 \rangle$) for $M_s \sim 0.5$, $\sim$1, and $\sim$3, respectively. In the right panel, cyan, black, and magenta solid (dashed) curves correspond to $B_0 = 0.001$, 0.01, and 0.1 for 256^3 (512^3) resolution, respectively. Only the finite-correlated driving is considered in the right panel.

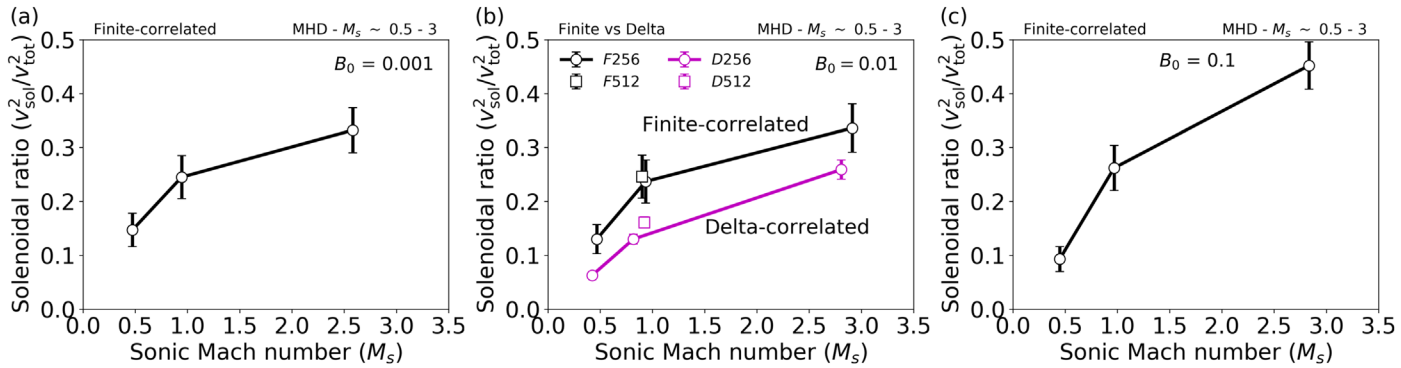

Figure 4. Average values of the solenoidal ratio (v_{sol}^2/v_{tot}^2) as a function of the sonic Mach number (M_s) for the MHD simulations with $B_0 \leqslant 0.1$. (a) $B_0 = 0.001$. (b) $B_0 = 0.01$. (c) $B_0 = 0.1$. In the left ($B_0 = 0.001$) and the right panels ($B_0 = 0.1$), we present the ratio of the finite-correlated compressive driving only. In the middle panel ($B_0 = 0.01$), black and magenta circles (squares) indicate the finite-correlated and the delta-correlated compressive drivings for 256^3 (512^3) resolution, respectively. Error bars in each panel denote standard deviations. In Table 1, the average values and the time intervals for taking average are shown.

respectively. The figure apparently presents that solenoidal ratios increase as M_s increases. When $M_s \sim 3$, the solenoidal ratio is $\sim$0.35. For comparison, Federrath et al. (2010), who used a finite-correlated driving, obtained a ratio of $\sim$0.4 in compressively driven HD turbulence at $M_s \sim 5$. The higher ratio they obtained may stem from having had a value of M_s that was higher than ours. On top of that, when M_s is similar, solenoidal ratios of the finite-correlated compressive driving are always higher than those of the delta-correlated compressive driving. Therefore, in HD turbulence driven by compressive driving, generation of solenoidal motions is dependent on both M_s and driving schemes.

3.2. Effects of the Sonic Mach Number in MHD Turbulence

Here, we mainly study how the sonic Mach number M_s influences generation of solenoidal motions in MHD turbulence driven by compressive driving. We study effects of driving schemes and numerical resolution as well. We consider weak mean magnetic field cases ($B_0 \leqslant 0.1$) in Section 3.2.1 and a strong mean magnetic field case ($B_0 = 1.0$) in Section 3.2.2.

3.2.1. Weak B_0 Cases ($B_0 \leqslant 0.1$)

Figures 3 shows time evolution of $\langle v_{tot}^2 \rangle$ and $\langle v_{sol}^2 \rangle$ in MHD turbulence driven by compressive driving. Blue, red, and green curves in Figures 3(a) and (b) correspond to $M_s \sim 0.5$, $\sim$1, and $\sim$3, respectively. We separately consider the finite-correlated and the delta-correlated compressive drivings in Figures 3(a) and (b), respectively. According to those two figures, the evolution of $\langle v_{tot}^2 \rangle$ is similar irrespective of M_s. However, the level of $\langle v_{sol}^2 \rangle$ at saturation increases as M_s increases in both driving schemes.

Figure 3(c) shows the effects of numerical resolution and B_0 in the case of $M_s \sim 1$ and the finite-correlated compressive driving. We plot the results of six simulations. In the figure, different colors of curves represent different values of B_0: cyan, black, and magenta colors correspond to $B_0 = 0.001$, 0.01, and 0.1, respectively. Each color has two different line styles: solid and dashed curves correspond to 256^3 and 512^3 resolutions, respectively. As in the case of HD turbulence, the resolution effect seems insignificant: in the figure, solid and dashed curves with the same color virtually coincide, which means that results are nearly resolution-independent. In addition, time evolution of all curves looks similar, which means that the effect of B_0 also seems insignificant for $M_s \sim 1$ and $B_0 \leqslant 0.1$ (see Section 3.3 for B_0 higher than 0.1).

Figure 4 shows the averaged solenoidal ratio as a function of M_s for simulations with $M_s \lesssim 3$ and $B_0 \leqslant 0.1$. Panels (a)–(c) in Figure 4 correspond to the ratios for $B_0 = 0.001$, 0.01, and 0.1, respectively. In Figure 4(a) and (c), we consider only the finite-correlated compressive driving. In Figure 4(b) (see the middle panel), black and magenta circles (squares) correspond to the finite-correlated and the delta-correlated compressive drivings for 256^3 (512^3) resolution, respectively.

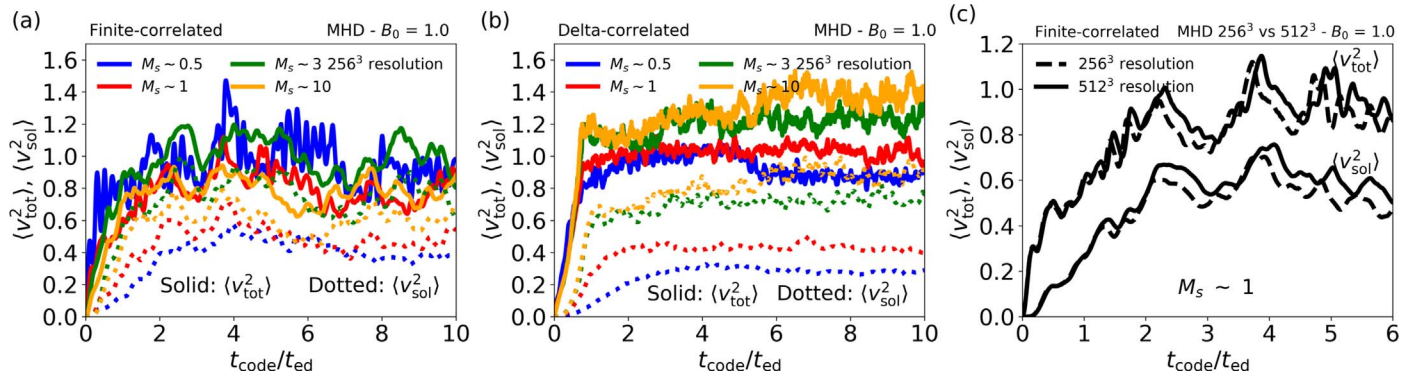

Figure 5. Similar to Figure 3, but for $B_0 = 1.0$. Blue, red, green, and orange curves in the left and the middle panels represent $M_s \sim 0.5$, ~ 1, ~ 3 and ~ 10, respectively. In the right panel, dashed and solid curves correspond to 256^3 and 512^3 resolutions for the finite-correlated compressive driving, respectively.

As in the case of HD turbulence, we can observe the following trends in Figure 4. First, for M_s effects, we can clearly see that as M_s increases, the solenoidal ratio also increases regardless of B_0. When $M_s \sim 3$, the ratio is as large as ~ 0.35 for $B_0 = 0.001$ and 0.01, and ~ 0.45 for $B_0 = 0.1$. The trend we observe is consistent with the result from Federrath et al. (2011), who considered a much lower mean magnetic field strength than ours and used a finite-correlated compressive driving. They obtained solenoidal ratios of ~ 0.10, ~ 0.27, and ~ 0.32 for $M_s \sim 0.5$, ~ 1.0, and ~ 3.0, respectively. Those values are similar to ours: ~ 0.13, ~ 0.24, and ~ 0.33 for similar values of M_s and $B_0 = 0.01$. This implies that the solenoidal ratio is not sensitive to B_0 as long as B_0 is sufficiently small (see Section 3.3 for further discussion). Second, as we showed in Figure 4(b), the solenoidal ratio does not seem sensitive to numerical resolution. This can also be supported by comparing the result of Porter et al. (2015) with ours. They forced turbulence using a delta-correlated compressive driving to have $M_s \sim 0.5$ and considered a mean magnetic field strength of $B_0 \sim 0.001$ in our units. The solenoidal ratio is ~ 0.07 in their simulation with a 1024^3 resolution. Taking into account the fact that the solenoidal ratio is insensitive to numerical resolution, we can conclude that their result is consistent with ours of ~ 0.06 from a 256^3 resolution (Run D256MS0.5-$B_0$0.01). Third, we can see from Figure 4(b) that, when M_s is similar and numerical resolution is same, the finite-correlated compressive driving results in a higher solenoidal ratio than does the delta-correlated compressive driving.

3.2.2. A Strong B_0 Case ($B_0 = 1$)

Figure 5 is similar to Figure 3, but we consider $B_0 = 1$ and M_s up to ~ 10. In Figures 5(a) and (b), blue, red, cyan, and orange solid (dotted) curves represent $\langle v_{tot}^2 \rangle$ ($\langle v_{sol}^2 \rangle$) for $M_s \sim 0.5$, ~ 1, ~ 3, and ~ 10, respectively. Panels (a) and (b) of Figure 5 are for the finite-correlated and the delta-correlated compressive drivings, respectively.

First of all, when we compare Figure 5 with Figure 3, we can note that the levels of $\langle v_{sol}^2 \rangle$ at saturation are much higher. Second, as we can see from Figure 5(a), the finite-correlated compressive driving yields similar levels of $\langle v_{tot}^2 \rangle$ irrespective of M_s. However, $\langle v_{sol}^2 \rangle$ shows dependence on M_s. Roughly speaking, the level of $\langle v_{sol}^2 \rangle$ increases as M_s increases for $M_s \lesssim 3$ (see Figure 6 for a more quantitative evaluation of this). Third, as we can see in Figure 5(b), the level of $\langle v_{sol}^2 \rangle$ increases with M_s for the delta-correlated compressive driving.

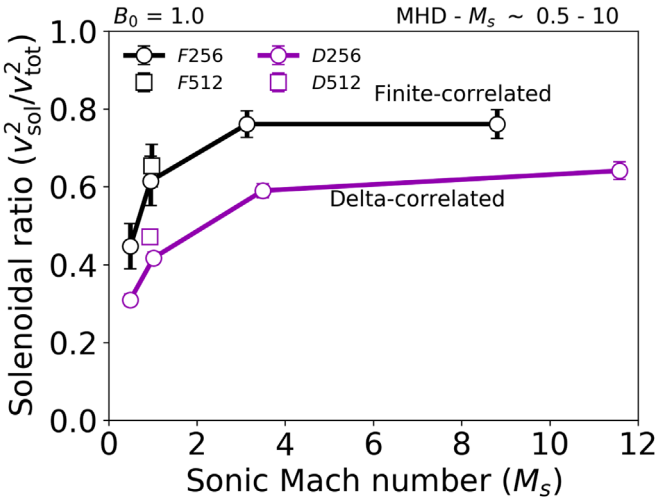

Figure 6. Same as Figure 4(b), but for $B_0 = 1.0$. We consider M_s up to ~ 10.

Figure 5(c) shows results of our resolution study for the finite-correlated compressive driving in the case of $M_s \sim 1$. Dashed and solid curves are for 256^3 and 512^3 resolutions, respectively. Similar to the case of $B_0 = 0.01$, the effect of resolution on $\langle v_{sol}^2 \rangle$ does not seem very significant.

Figure 6 shows the solenoidal ratio as a function of M_s for $B_0 = 1.0$. Black and magenta circles (squares) correspond to the finite-correlated and the delta-correlated compressive drivings for 256^3 (512^3) resolution, respectively. In the figure, we can observe the same trend of the solenoidal ratio as in Figures 2 and 4; the ratio increases with M_s and is larger for the finite-correlated compressive driving than for the delta-correlated compressive driving at a similar M_s. It is worth noting that the solenoidal ratio exceeds 0.5 for both driving schemes in the supersonic regime. This means that, although turbulence is driven by compressive driving, solenoidal modes eventually dominate over compressive ones in the presence of a strong mean magnetic field. This result may imply that Alfvén modes become more important than compressive modes in the regime.

3.3. Effects of the Mean Magnetic Field

In this subsection, we deal with effects of the mean magnetic field (B_0) on the generation of solenoidal modes in turbulence driven by compressive driving. For this purpose, we consider $M_s \lesssim 3$ and B_0 ranging from 0.001 (very weak mean field case)

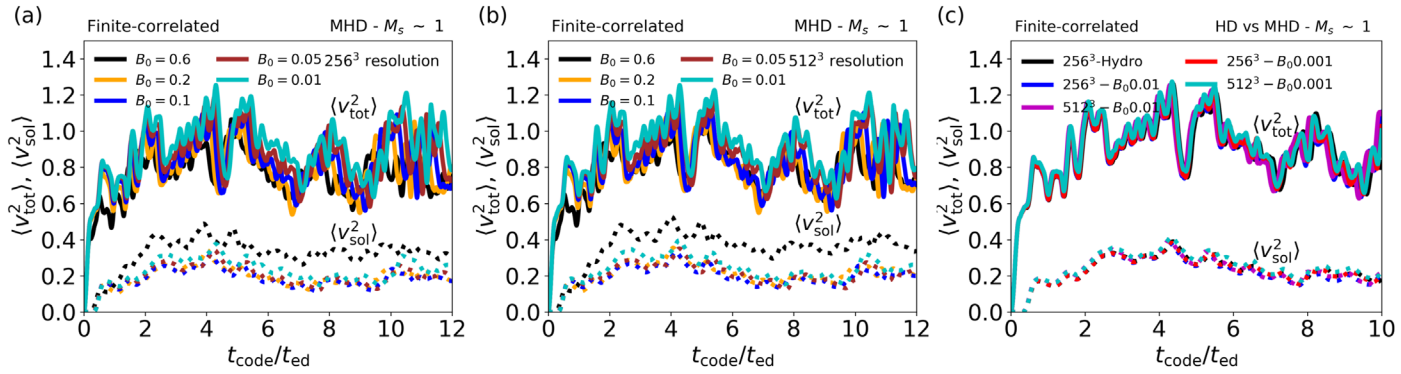

Figure 7. Time evolution of $\langle v_{tot}^2 \rangle$ (solid curves) and $\langle v_{sol}^2 \rangle$ (dotted curves) for MHD turbulence simulations with $M_s \sim 1$. (a) Finite-correlated compressive driving with 256^3 resolution. (b) Finite-correlated compressive driving with 512^3 resolution. (c) Comparison of HD and MHD simulations. Cyan, brown, blue, orange, and black curves in left and middle panels represent $B_0 = 0.01$, 0.05, 0.1, 0.2, and 0.6, respectively. In the right panel, black curves represent Run F256MS1-Hydro simulation. Blue and magenta curves correspond to Run F256MS1-$B_0$0.01 and Run F512MS1-$B_0$0.01, respectively. Red and cyan curves correspond to Run F256MS1-$B_0$0.001 and Run F512MS1-$B_0$0.001, respectively.

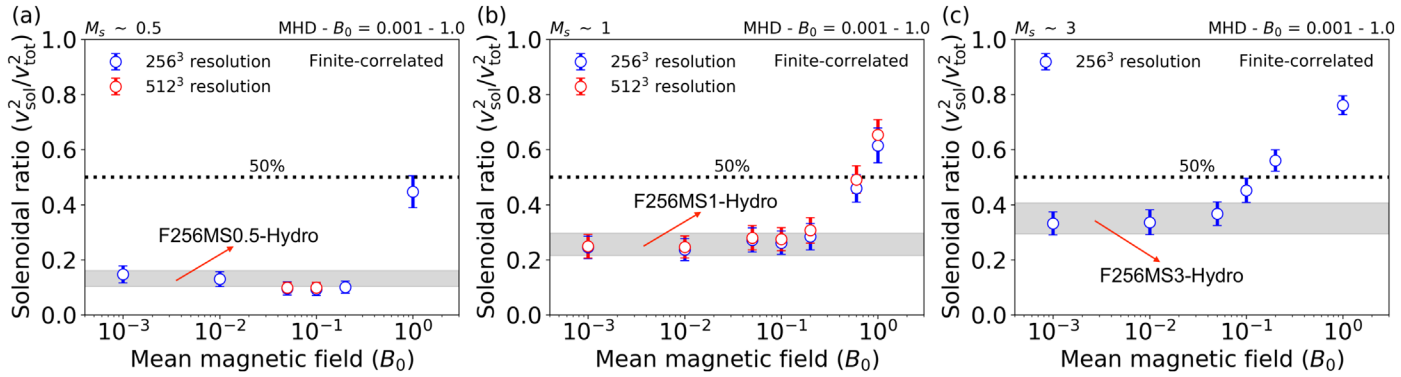

Figure 8. Average values of the solenoidal ratio (v_{sol}^2/v_{tot}^2) as a function of the mean magnetic field (B_0) for the MHD simulations with $M_s \lesssim 3$. (a) $M_s \sim 0.5$. (b) $M_s \sim 1$. (c) $M_s \sim 3$. In the right panel ($M_s \sim 3$), we present results from 256^3 resolution simulations only. In the left and the middle panels, blue and red circles denote the solenoidal ratios of the simulations with 256^3 and 512^3 resolutions, respectively. Gray shaded region in each panel shows the 1σ dispersion about the average ratio from HD simulations. Error bars show standard deviations. In Table 1, the average values and the time intervals for taking average are shown.

to 0.6 (marginally strong mean field case). We do not study effects of driving schemes here; we consider only the finite-correlated compressive driving.

Figure 7 shows time evolution of $\langle v_{tot}^2 \rangle$ and $\langle v_{sol}^2 \rangle$ in MHD turbulence driven by compressive driving. Cyan, brown, blue, orange, and black curves in Figures 7(a) and (b) correspond to $B_0 = 0.01$, 0.05, 0.1, 0.2, and 0.6, respectively. The numerical resolutions in panels (a) and (b) of Figure 7 are 256^3 and 512^3, respectively. Figure 7(c) shows simulation results for $B_0 \leqslant 0.01$, in which magenta, blue, cyan, red, and black curves correspond to Run F512MS1-$B_0$0.01, Run F256MS1-$B_0$0.01, Run F512MS1-$B_0$0.001, Run F256MS1-$B_0$0.001, and Run F256MS1-Hydro, respectively. Note that all solid curves virtually coincide and so do all dotted curves.

First, $\langle v_{tot}^2 \rangle$ and $\langle v_{sol}^2 \rangle$ for all simulations in Figure 7 seem to saturate roughly after $3t_{ed}$. Second, in Figure 7(a) and (b), the evolution of $\langle v_{tot}^2 \rangle$ is almost same irrespective of both B_0 and the numerical resolution. Furthermore, when $B_0 \leqslant 0.2$, the evolution of $\langle v_{sol}^2 \rangle$ at saturation is nearly indistinguishable in both numerical resolutions (i.e., in both Figure 7(a) and (b)). On the other hand, the level of $\langle v_{sol}^2 \rangle$ for $B_0 = 0.6$ at saturation is notably higher than those for $B_0 \leqslant 0.2$ in both numerical resolutions. Third, according to Figure 7(c), it is noticeable that both numerical resolution and the degree of magnetization do not strongly affect the evolutions of $\langle v_{tot}^2 \rangle$ and $\langle v_{sol}^2 \rangle$ when B_0 is weak or zero.

Figure 8 shows average values of the solenoidal ratio as a function of B_0. Panels (a)–(c) in Figure 8 correspond to the ratios for $M_s \sim 0.5$, ~1, and ~3, respectively. In Figure 8(c), we present the results of simulations with 256^3 resolution only. In Figure 8(a) and (b), blue and red circles represent 256^3 and 512^3 resolutions, respectively. The gray shaded region in each panel indicates the 1σ dispersion about the average solenoidal ratio from the HD simulations.

First, Figure 8 clearly shows that the solenoidal ratio is lower when M_s is lower at the same B_0, as we discussed earlier in Sections 3.1 and 3.2. Second, when B_0 is small, the solenoidal ratio is virtually the same as the HD value. However, as B_0 exceeds a certain strength, the ratio begins to deviate from the HD value. The solenoidal ratio seems to exceed 0.5 when $B_0 \geqslant 0.6$ for $M_s \sim 1$ and $B_0 \geqslant 0.2$ for $M_s \sim 3$. Third, we note that deviation of the ratio from the HD values occurs roughly at $B_0 = 0.1$. However, it shows a weak dependence on M_s. When $M_s \lesssim 1$, the solenoidal ratios for $B_0 \leqslant 0.2$ are not considerably different from the ratio of the HD simulations. On the contrary, in the case of $M_s \sim 3$, this happens at a smaller B_0 (~0.05). Last, in Figure 8(a) and (b), the numerical resolution does not seem to have substantial impacts on the ratio, especially for $B_0 \leqslant 0.1$. Although the ratio slightly depends on numerical resolution, the difference is within the error bar.

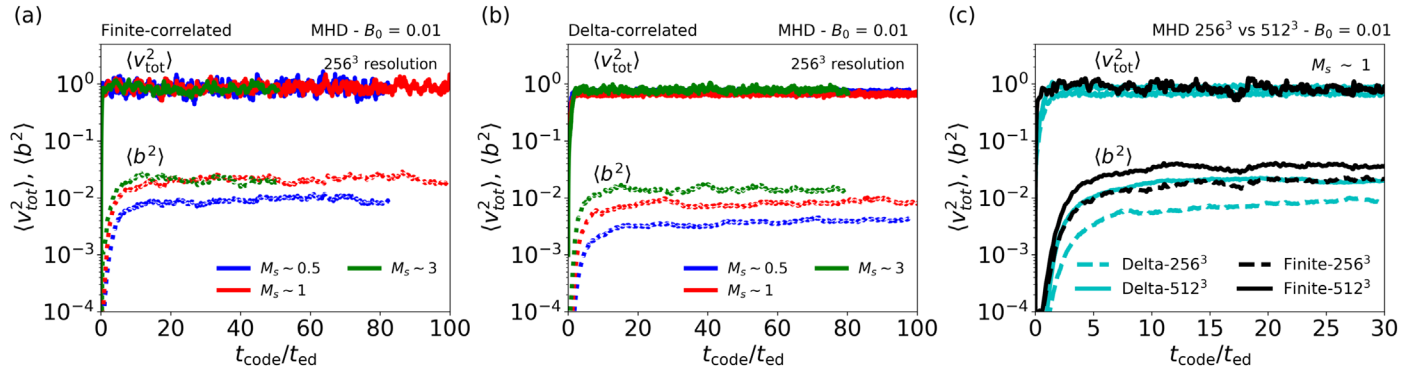

Figure 9. Time evolution of $\langle v_{tot}^2 \rangle$ and $\langle b^2 \rangle$ for MHD turbulence simulations with $B_0 = 0.01$. (a) Finite-correlated compressive driving. (b) Delta-correlated compressive driving. (c) Resolution study for both the finite-correlated and the delta-correlated compressive drivings in the case of $M_s \sim 1$. Blue, red, and green solid (dotted) curves in the left and the middle panels represent $\langle v_{tot}^2 \rangle$ ($\langle b^2 \rangle$) for $M_s \sim 0.5$, $\sim$1, and $\sim$3, respectively. In the right panel, black dashed and solid curves correspond to 256^3 and 512^3 resolutions for the finite-correlated compressive driving, respectively. Cyan dashed and solid curves correspond to 256^3 and 512^3 resolutions for the delta-correlated compressive driving, respectively. For $\langle b^2 \rangle$, the red dotted curves in the left and the middle panels are the same as the black dashed and cyan dashed curves in the right panel, respectively.

4. Generation of Small-scale Random Magnetic Fields

In this section, we investigate the generation of small-scale magnetic field in compressively driven turbulence. The strength of the small-scale magnetic field is defined by $b = \sqrt{B^2 - B_0^2}$ as we described in Section 2. At the beginning of simulations, no random magnetic field exists. Then, as simulations go on, turbulence develops and amplifies small-scale magnetic field via the stretching effect, which is mainly provided by the solenoidal velocity component. In Sections 4.1 and 4.2, we deal with the effects of the sonic Mach number (M_s) and the mean magnetic field (B_0), respectively.

4.1. Effects of the Sonic Mach Number

4.1.1. Weak B_0 Cases ($B_0 = 0.01$)

Figure 9 shows the time evolution of $\langle v_{tot}^2 \rangle$ and $\langle b^2 \rangle$ in MHD turbulence driven by compressive driving. Blue, red, and green curves in Figure 9(a) and (b) correspond to $M_s \sim 0.5$, $\sim$1, and $\sim$3, respectively. Figures 9(a) and (b) are for the finite-correlated and the delta-correlated compressive drivings, respectively. Figure 9(c) shows results of resolution study. In the figure, different colors of curves represent different driving schemes and different line styles different numerical resolutions. Black dashed and black solid curves indicate the finite-correlated compressive driving for 256^3 and 512^3 resolutions, respectively. Cyan dashed and cyan solid curves indicate the delta-correlated compressive driving for 256^3 and 512^3 resolutions, respectively. The vertical axis is in logarithmic scale in all panels.

First of all, panels (a) and (b) of Figure 9 obviously reveal the effect of M_s on the growth of $\langle b^2 \rangle$: although the level of $\langle v_{tot}^2 \rangle$ at saturation is almost identical regardless of M_s, that of $\langle b^2 \rangle$ depends on M_s. When we compare $\langle b^2 \rangle$ for $M_s \sim 0.5$ (see the blue dotted curves) and $\sim$1 (see the red dotted curves) in those figures, the values for $M_s \sim 1$ are larger. However, when we compare $\langle b^2 \rangle$ for $M_s \sim 1$ and $\sim$3 (see the green dotted curves), the behaviors of the finite-correlated (left panel) and the delta-correlated (middle panel) drivings are different: the finite-correlated compressive driving yields similar level of $\langle b^2 \rangle$ between $M_s \sim 1$ and $\sim$3, while the delta-correlated compressive driving produces larger $\langle b^2 \rangle$ for $M_s \sim 3$. Second, both panel (a) and panel (b) have a common feature: $\langle b^2 \rangle$ grows fast when $t \lesssim 5$ and it gradually levels off when $t \gtrsim 5$. In some simulations, $\langle b^2 \rangle$ reaches saturation level relatively quickly, while in others, it does more or less slowly. Finally, as opposed to the case of $\langle v_{sol}^2 \rangle$, Figure 9(c) clearly shows resolution dependence of $\langle b^2 \rangle$, with the level of $\langle b^2 \rangle$ at saturation being increasing with the numerical resolution for both driving schemes. Previous numerical studies reported such a resolution effect on turbulence dynamos for solenoidally driven turbulence: for the case of incompressible MHD turbulence, see, e.g., Cho et al. (2009); for compressible MHD turbulence, see, e.g., Ryu et al. (2008).

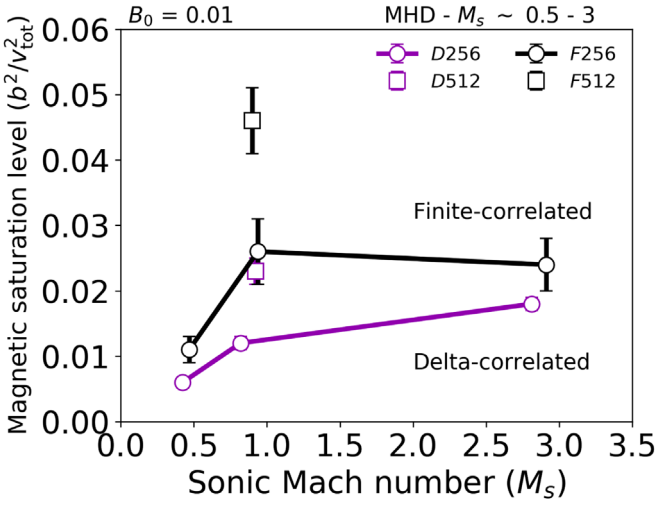

Figure 10. Averaged values of the magnetic saturation level (b^2/v_{tot}^2) as a function of the sonic Mach number (M_s) for $B_0 = 0.01$. Black and magenta circles (squares) indicate the finite-correlated and the delta-correlated compressive drivings for 256^3 (512^3) resolution, respectively. The error bars represent standard deviations. In Table 1, the average values and the time intervals for taking average are shown.

Figure 10 summarizes the results from Figure 9. The figure shows the magnetic saturation level as a function of M_s. Black and magenta circles (squares) correspond to the finite-correlated and the delta-correlated compressive drivings at 256^3 (512^3) resolution, respectively. The magnetic saturation level is clearly dependent on M_s, driving schemes, and the numerical resolution. First, for the range of M_s presented in Figure 10, the two driving schemes show different behaviors

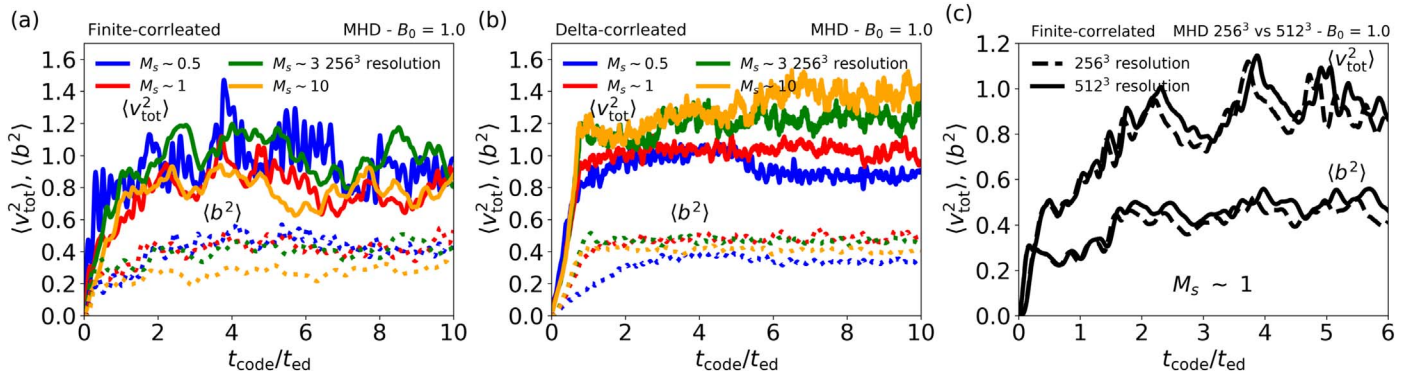

Figure 11. Similar to Figure 9, but for $B_0 = 1.0$. Blue, red, green, and orange curves in the left and the middle panels represent $M_s \sim 0.5$, ~ 1, ~ 3, and ~ 10, respectively. In the right panel, dashed and solid curves correspond to 256^3 and 512^3 resolutions for the finite-correlated compressive driving, respectively.

when we fix the numerical resolution: although it keeps increasing as M_s increases for the delta-correlated compressive driving, it is not the case for the finite-correlated compressive driving. That is, the magnetic saturation level for the finite-correlated compressive driving peaks at $M_s \sim 1$ and slightly decreases for $M_s \gtrsim 1$. Second, for the same numerical resolution, we can clearly see that the finite-correlated compressive driving yields a larger magnetic saturation level than the delta-correlated compressive driving at a similar M_s. Third, when we compare the magnetic saturation level for 256^3 and 512^3 resolutions, it is larger for the latter resolution.

4.1.2. *Strong* B_0 *Cases* ($B_0 = 1$)

Figure 11 shows time evolution of $\langle v_{tot}^2 \rangle$ and $\langle b^2 \rangle$ for $B_0 = 1$. We consider the finite-correlated and the delta-correlated compressive drivings separately in Figure 11(a) and (b), respectively. In the figures, blue, red, cyan, and orange solid (dotted) curves represent $\langle v_{tot}^2 \rangle$ ($\langle b^2 \rangle$) for $M_s \sim 0.5$, ~ 1, ~ 3, and ~ 10, respectively. The levels of $\langle b^2 \rangle$ at saturation in the figures are not very sensitive to M_s for both driving schemes. Figure 11(c) shows results of resolution study for the finite-correlated compressive driving in the case of $M_s \sim 1$. Dashed and solid curves denote 256^3 and 512^3 numerical resolutions, respectively. We can see from Figure 11(c) that the resolution effect on $\langle b^2 \rangle$ is not very significant.

Figure 12 shows the magnetic saturation level as a function of M_s for $B_0 = 1.0$. Black and magenta circles (squares) correspond to the finite-correlated and the delta-correlated compressive drivings for 256^3 (512^3) resolution, respectively. Although weak, the magnetic saturation level shows dependence on M_s: it goes up as M_s increases when $M_s \lesssim 1$ and it decreases as M_s increases when $M_s \gtrsim 1$ for both driving schemes. In addition, numerical resolution effect on the magnetic saturation level is hardly pronounced especially for the finite-correlated compressive driving.

4.2. *Effects of the Mean Magnetic Field*

In this subsection, we deal with the effect of the mean magnetic field B_0 on small-scale dynamo in turbulence driven by compressive driving. Figure 13 shows time evolution of $\langle v_{tot}^2 \rangle$ (solid curves) and $\langle b^2 \rangle$ (dotted curves) for different mean magnetic field strengths for the finite-correlated compressive driving. From left to right, panels (a)–(c) are for $M_s \sim 0.5$, ~ 1, and ~ 3, respectively. Cyan, brown, blue, orange, and black curves in each panel indicate $B_0 = 0.01$, 0.05, 0.1, 0.2, and 0.6,

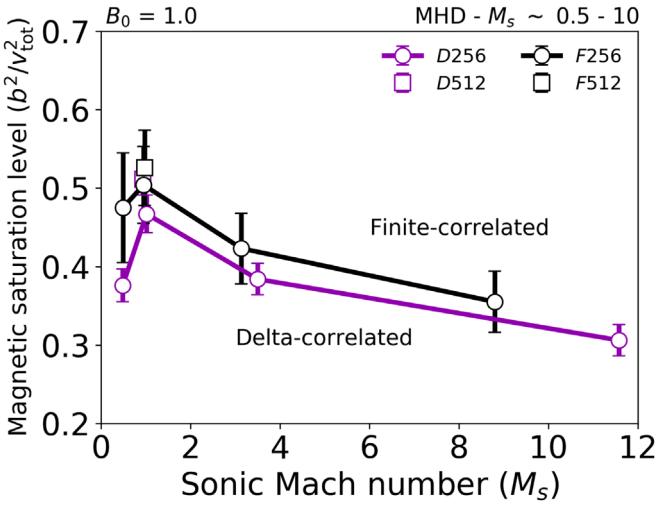

Figure 12. Same as Figure 10, but for $B_0 = 1.0$. We consider M_s up to ~ 10.

respectively. Note that we present results for various values of B_0 in each panel. The vertical axis is in logarithmic scale in all panels. As we can see from the figure, the level of $\langle b^2 \rangle$ at saturation increases with B_0 for all values of M_s. In general, when B_0 is weaker, the saturation level is lower and it takes more time to reach it.

In Figure 14, we present time evolutions of $\langle v_{tot}^2 \rangle$ and $\langle b^2 \rangle$ from additional MHD simulations with either higher numerical resolutions or different values of B_0. In Figure 14(a), we present results for 512^3 resolution. In Figure 14(b), we present results for $B_0 = 0.001$. In Figure 14(c), we compare the effects of numerical resolution for fixed B_0 and M_s.

Figure 14(a) is the same as Figure 13(b), but for 512^3 resolution: in this figure, cyan, brown, blue, orange, and black solid (dotted) curves denote time evolution of $\langle v_{tot}^2 \rangle$ ($\langle b^2 \rangle$) for $B_0 = 0.01$, 0.05, 0.1, 0.2, and 0.6 at $M_s \sim 1$, respectively. We can clearly see almost the same evolutions of both $\langle v_{tot}^2 \rangle$ and $\langle b^2 \rangle$ as those for 256^3 resolution (compare Figure 14(a) with Figure 13(b)). However, 512^3 resolution gives slightly higher saturation values of $\langle b^2 \rangle$ than 256^3 resolution (see Figure 15 for details).

Figure 14(b) simultaneously shows effects of both M_s and numerical resolution on $\langle b^2 \rangle$ in the case of $B_0 = 0.001$. In this figure, blue solid, red solid, and green solid curves correspond to $M_s \sim 0.5$, ~ 1, and ~ 3 for 256^3 resolution, respectively. Red dotted curves are for 512^3 resolution in the case of $M_s \sim 1$. First of all, the time evolution of $\langle b^2 \rangle$ for $M_s \sim 0.5$ clearly

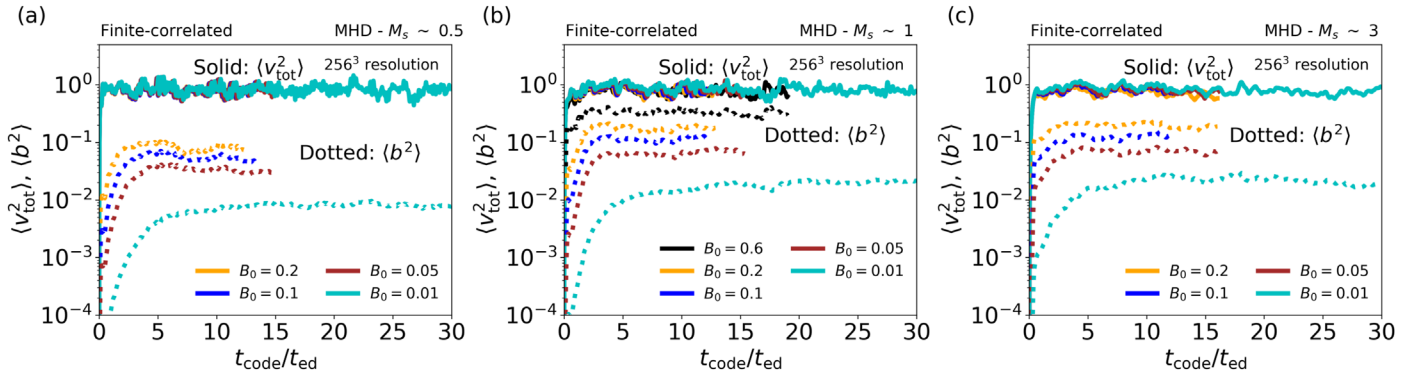

Figure 13. Time evolution of $\langle v_{tot}^2 \rangle$ (solid curves) and $\langle b^2 \rangle$ (dotted curves) for MHD turbulence simulations with 256^3 resolution and $M_s \lesssim 3$. (a) $M_s \sim 0.5$. (b) $M_s \sim 1$. (c) $M_s \sim 3$. In each panel, cyan, brown, blue, orange, and black curves represent $B_0 = 0.01$, 0.05, 0.1, 0.2, and 0.6, respectively.

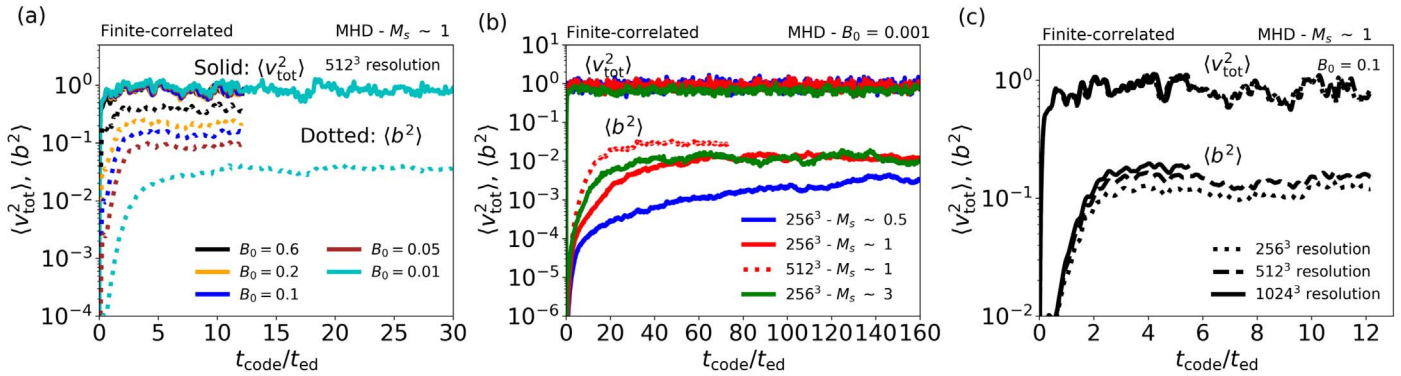

Figure 14. Time evolutions of $\langle v_{tot}^2 \rangle$ and $\langle b^2 \rangle$ for MHD turbulence simulations with high numerical resolutions and different values of B_0. (a) Same as Figure 13(b), but for 512^3 resolution. (b) Comparison for M_s and numerical resolution effects in the case of $B_0 = 0.001$. Solid curves with blue, red, and green colors represent $M_s \sim 0.5$, ~1, and ~3 for 256^3 resolution, respectively. Red dotted curves denote 512^3 resolution simulation with $M_s \sim 1$. (c) Resolution study only for $B_0 = 0.1$ and $M_s \sim 1$. Dotted, dashed, and solid curves indicate 256^3, 512^3, and 1024^3 resolutions, respectively.

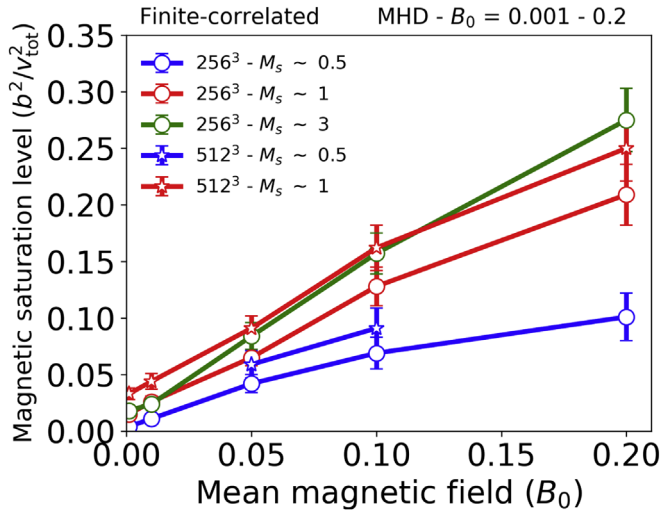

Figure 15. Average values of the magnetic saturation level as a function of the mean magnetic field (B_0) for MHD turbulence simulations with $M_s \lesssim 3$ and $B_0 \leqslant 0.2$. Circles with blue, red, and green colors represent 256^3 resolution simulations with $M_s \sim 0.5$, ~1, and ~3, respectively. Blue and red stars denote 512^3 resolution simulations with $M_s \sim 0.5$ and ~1, respectively. Error bars show standard deviations. In Table 1, the average values and the time intervals for taking an average are shown.

shows slower growth of $\langle b^2 \rangle$ compared to that of $M_s \sim 1$ and ~3: $\langle b^2 \rangle$ for $M_s \gtrsim 1$ saturates roughly after $60t_{ed}$, but that for $M_s \sim 0.5$ grows until $140t_{ed}$. Furthermore, the level of $\langle b^2 \rangle$ at saturation is similar between $M_s \sim 1$ and ~3, and that for $M_s \sim 0.5$ is lower. Second, when we compare the time evolution of $\langle b^2 \rangle$ for 256^3 and 512^3 resolutions at $M_s \sim 1$ (see red solid and red dotted curves in Figure 14(b)), it is obvious that the $\langle b^2 \rangle$ of the latter resolution grows faster and exhibits a higher level of $\langle b^2 \rangle$ than that of the former resolution.

Figure 14(c) shows a resolution study for the case of $B_0 = 0.1$ and $M_s \sim 1$. Dotted, dashed, and solid curves indicate 256^3, 512^3, and 1024^3 resolutions, respectively. According to the figure, three different resolution simulations produce almost the same time evolution of $\langle v_{tot}^2 \rangle$. On the other hand, a simulation with a higher numerical resolution results in a higher level of $\langle b^2 \rangle$ at saturation. However, we can clearly see that the change of the level of $\langle b^2 \rangle$ at saturation with numerical resolution is not significant in compressively driven turbulence.

Figure 15 denotes the magnetic saturation level as a function of B_0 for the simulations with $M_s \lesssim 3$. Blue, red, and green circles indicate $M_s \sim 0.5$, ~1, and ~3 for 256^3 resolution, respectively. Blue and red stars correspond to $M_s \sim 0.5$ and ~1 for 512^3 resolution, respectively. The figure reveals an approximately linear relation between B_0 and the magnetic saturation level,

$$\langle b^2 \rangle / \langle v_{tot}^2 \rangle = cB_0 + d, \quad (5)$$

regardless of M_s and numerical resolution. Here, c and d are constants with proper dimensions. If we compare circles (256^3) and stars (512^3) at the same M_s (i.e., the same color), we can clearly see that 512^3 resolution gives higher saturation levels than 256^3 resolution. The slopes of the linear relation are very

similar for both resolutions. Note, however, that the increase of the magnetic saturation level with numerical resolution is not significant compared to that for solenoidally driven turbulence (see Section 6 for further discussion). If we compare results for different values of M_s, the slope becomes slightly steeper as M_s increases at the same numerical resolution.

5. Discussion on Solenoidal Ratio

In Section 3, we have studied the effects of both the sonic Mach number (M_s) and the mean field strength (B_0) on the generation of solenoidal velocity components in compressively driven turbulence. We have found that the solenoidal component produced by compressive driving is dependent on M_s and B_0. In addition, when M_s is similar and the numerical resolution is same, the finite-correlated compressive driving generates a greater solenoidal velocity component than does the delta-correlated compressive driving. We discuss these findings and their implications in this section.

5.1. Dependence of Solenoidal Ratio on M_s and B_0

Let us discuss how larger M_s and B_0 result in a higher solenoidal ratio. To study the generation of solenoidal velocity components, it is helpful to write down the vorticity equation,[4] "which is obtained from the curl of the Navier–Stokes equation with magnetic (Maxwell) stresses, $\boldsymbol{j} \times \boldsymbol{B}$, added" (Porter et al. 2015):

$$\frac{\partial \boldsymbol{w}}{\partial t} = -\nabla \cdot (\boldsymbol{v}w) + (\boldsymbol{w} \cdot \nabla)\boldsymbol{v} + \frac{1}{\rho^2}\nabla\rho \times \nabla P_T + \nabla \times \left(\frac{\boldsymbol{T}}{\rho}\right) + \nu(\nabla^2 w + \nabla \times \boldsymbol{G}) + \nabla \times \boldsymbol{f}, \quad (6)$$

where $\boldsymbol{w}$ ($=\nabla \times \boldsymbol{v}$) is the vorticity, P_T ($=p + P_B$) is the sum of the gas pressure, p, and the magnetic pressure, $P_B = (1/2)B^2$, $\boldsymbol{T}$ ($= \boldsymbol{B} \cdot \nabla \boldsymbol{B}$) is the magnetic tension, and ν is the kinematic viscosity. In the viscous term, $\boldsymbol{G}$ is defined by $\boldsymbol{G} = (1/\rho)\nabla\rho \cdot \boldsymbol{S}$, where $\boldsymbol{S}$ is the standard traceless strain tensor (see, e.g., Mee & Brandenburg 2006).

In our simulations, velocity and hence vorticity are zero at the beginning. How then is vorticity generated later on? We note that the last term on the right-hand side (rhs) in Equation (6) is zero in our simulations with compressive driving. In addition, since we assume the isothermal equation of state, $p \propto \rho$, the baroclinic source term by gas pressure, $(1/\rho^2)(\nabla\rho \times \nabla p)$, where p is the gas pressure, vanishes. Next, let us first assume that B_0 is zero or extremely small. In this case, all terms except the viscous term (the penultimate term in Equation (6)), on the rhs are either exactly zero or almost zero when time is small. Our numerical simulations are for ideal MHD, such that ν is formally zero. However, on the grid resolution–scale, numerical dissipation can resemble the viscosity, which makes it possible for the viscous term to act numerically. Therefore, the viscous term can seed the vorticity across density gradients even in the absence of initial vorticity in compressively driven turbulence (Mee & Brandenburg 2006; Federrath et al. 2011). If B_0 is not very small, it is possible that the fourth term on the rhs generates vorticity even from the beginning.[5] Once seed vorticity is generated, the second term on the rhs can contribute to amplification of vorticity.

Here, we quantify the following source/amplification terms: the vortex stretching term, $(\boldsymbol{w} \cdot \nabla)\boldsymbol{v}$, the magnetic pressure term, $(1/\rho^2)(\nabla\rho \times \nabla P_B)$, and the magnetic tension term, $\nabla \times (\boldsymbol{T}/\rho)$. We consider only the finite-correlated compressive driving in this subsection.

Figure 16 shows PDFs of the source terms of vorticity for Run F512MS1-$B_0$0.01 (upper panels) and Run F512MS1-$B_0$1 (lower panels). Dotted, dashed, and solid curves in each panel denote the logarithms of the vortex stretching, magnetic pressure, and magnetic tension terms, respectively. The left and the right panels correspond to the PDFs calculated before and after saturation, respectively. We show the time at which each PDF is calculated in the left side of each panel.

We can note from the figure that the magnetic pressure and tension effects are not dominant in the case of $B_0 = 0.01$ (see dashed and solid curves in the upper panels); the former is weakest, and the latter is comparable to the stretching effect irrespective of whether turbulence saturates or not. On the other hand, in the case of $B_0 = 1$, we can clearly see that the magnetic tension effect is strongest, and the other two effects are weaker than the tension term and comparable with each other. Hence, we can suggest that, when B_0 is very strong, the magnetic tension effect is highly effective in generating vorticity and the solenoidal velocity component. In fact, we can explain the trend in Figure 8(b) in terms of the magnetic tension term: as B_0 increases, the magnetic tension effect increases, which in turn produces a greater solenoidal velocity component.

Figure 17 illustrates the effect of M_s on the vorticity equation for 256^3 resolution and $B_0 \leqslant 0.6$. From left to right, panels (a)–(c) show the average values of $\langle|\frac{1}{\rho^2}\nabla\rho \times \nabla P_B|\rangle$, $\langle|\nabla \times \frac{\boldsymbol{T}}{\rho}|\rangle$, and $\langle|(\boldsymbol{w} \cdot \nabla)\boldsymbol{v}|\rangle$ at saturation, respectively. In each panel, blue, red, and green circles correspond to $M_s \sim 0.5$, ~ 1, and ~ 3, respectively. The horizontal axis in each panel is total magnetic energy density (B^2).

First, we can clearly note that the magnetic pressure and tension terms are roughly proportional to B^2 for all values of M_s, with those for $M_s \sim 3$ being especially sensitive to B^2. This is understandable because the former contains B^2 and the latter $\boldsymbol{B} \cdot \nabla \boldsymbol{B}$. Second, according to Figure 17(c), the vortex stretching term does not show strong dependence on B^2 for all values of M_s. More precisely, it stays nearly constant when $B^2 \lesssim 0.1$ and deviates slightly from the constant when $B^2 > 0.1$. Third, if we compare the scales of the vertical axes in those panels, the magnetic tension term is the largest, in general. Last, the middle panel of Figure 17 shows that the magnetic tension term is larger when M_s is larger, which means that compressively driven turbulence with a higher M_s can generate vorticity more efficiently than that with a lower M_s, mainly via the magnetic tension effect.

Figures 18 and 19 are for the examination of the effect of B_0 in the case of $M_s \sim 1$ and 512^3 resolution. In those figures,

[4] As noted by Porter et al. (2015), the solenoidal velocity component and the vorticity are not exactly same. While the former, $v_{\rm sol} \propto l^{1/3}$, is dominant at the energy-injection scale, the latter, $w \propto l^{-2/3}$, concentrates near the dissipation scale, where l is a scale in the inertial range and $v_{\rm sol}$ and w are solenoidal velocity and vorticity associated with the scale, respectively. However, since the vorticity is essentially solenoidal and the generation of vorticity is accompanied by that of solenoidal velocity, we expect that the vorticity equation can trace the generation of the solenoidal velocity component.

[5] At $t = 0$, the magnetic tension ($\boldsymbol{T}$) is zero. Therefore, the fourth term on the rhs of Equation (6) is zero at $t = 0$. However, as soon as magnetic field lines are perturbed by turbulent motions, the tension term begins to work.

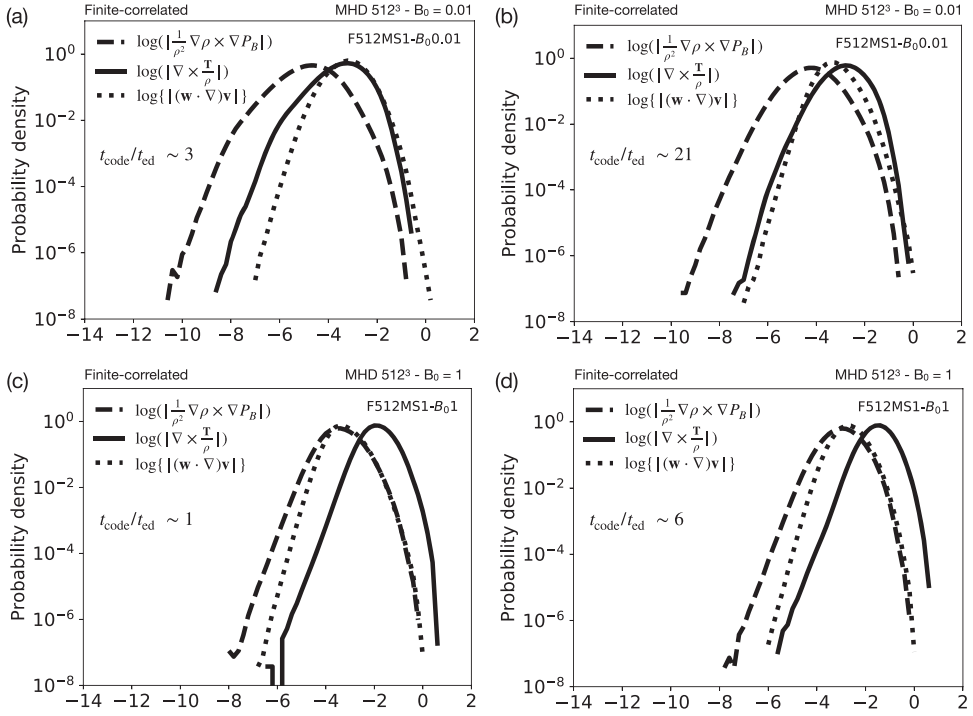

Figure 16. PDFs of $\log(|\frac{1}{\rho^2}\nabla\rho\times\nabla P_B|)$ (dashed curves), $\log(|\nabla\times\frac{\boldsymbol{T}}{\rho}|)$ (solid curves), and $\log\{|(\boldsymbol{w}\cdot\nabla)\boldsymbol{u}|\}$ (dotted curves) for MHD simulations with $M_s\sim 1$ and 512^3 resolution in the case of the finite-correlated compressive driving. Upper panels: $B_0 = 0.01$. Lower panels: $B_0 = 1.0$. PDFs in the left panels are calculated before saturation, and those in the right panels after saturation. Time at which each PDF is calculated is shown in each panel.

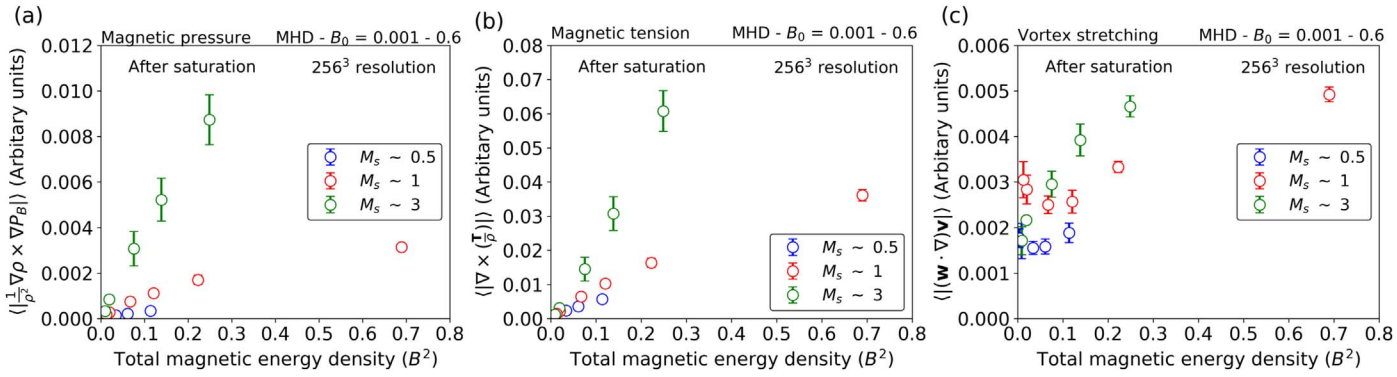

Figure 17. Average values of $\langle|\frac{1}{\rho^2}\nabla\rho\times\nabla P_B|\rangle$ (left panel), $\langle|\nabla\times\frac{\boldsymbol{T}}{\rho}|\rangle$ (middle panel), and $\langle|(\boldsymbol{w}\cdot\nabla)\boldsymbol{v}|\rangle$ (right panel) for MHD simulations with 256^3 resolution and $B_0\leqslant 0.6$ as a function of total magnetic energy density (B^2). Blue, red, and green circles in each panel denote $M_s\sim 0.5$, $\sim$1, and $\sim$3, respectively. Error bars represent standard deviations. We take the average values after saturation.

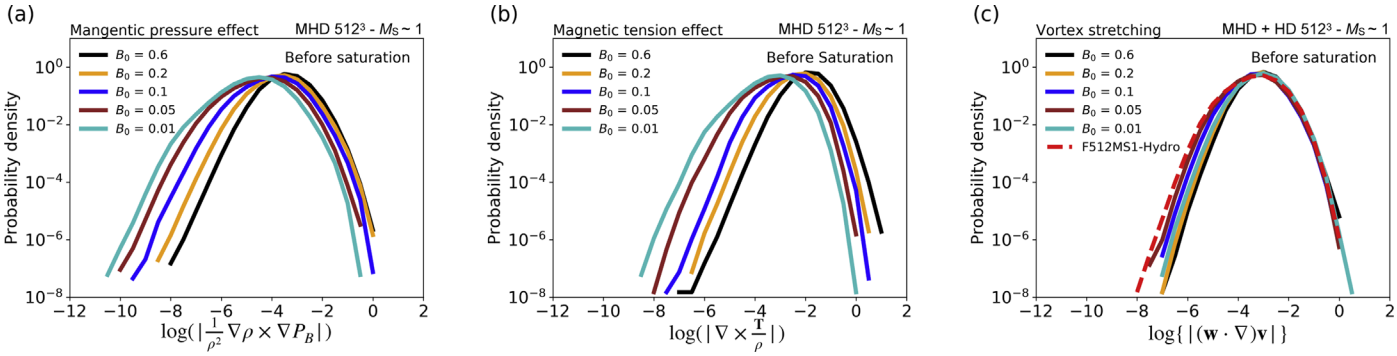

Figure 18. PDFs of $\log(|\frac{1}{\rho^2}\nabla\rho\times\nabla P_B|)$ (left panel), $\log(|\nabla\times\frac{\boldsymbol{T}}{\rho}|)$ (middle panel), and $\log\{|(\boldsymbol{w}\cdot\nabla)\boldsymbol{v}|\}$ (right panel) for MHD simulations with $M_s\sim 1$ and 512^3 resolution. Cyan, brown, blue, orange, and black curves in each panel represent $B_0 = 0.01$, 0.05, 0.1, 0.2, and 0.6, respectively. In the right panel, red dashed curve indicates the HD simulation, F512MS1-Hydro. PDFs are calculated before saturation.

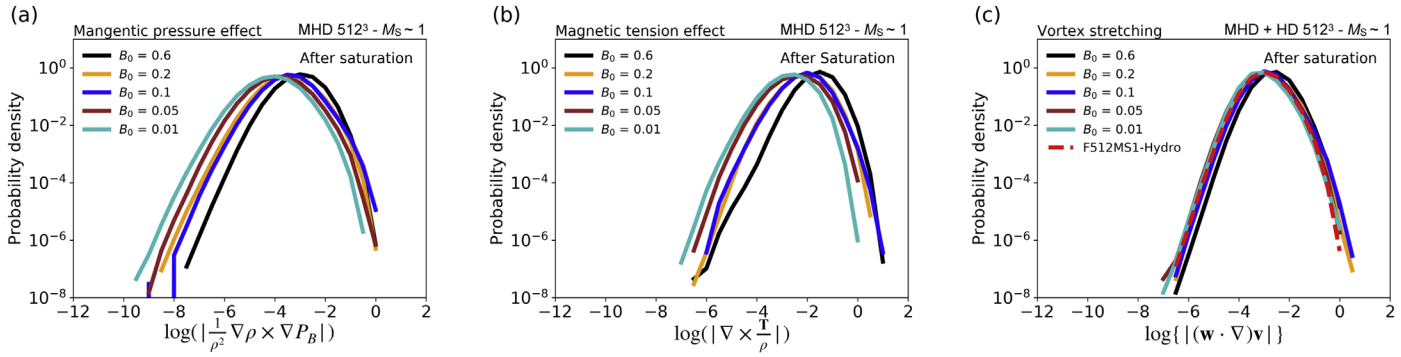

Figure 19. Same as Figure 18, but for PDFs calculated after saturation.

cyan, brown, blue, orange, and black curves correspond to $B_0 = 0.01, 0.05, 0.1, 0.2$, and 0.6, respectively. The red dashed lines in the right panels represent the HD simulation, Run F512MS1-Hydro. The PDFs before saturation are drawn in Figure 18 and those after saturation in Figure 19. It is obvious from the figures that the PDFs for the magnetic pressure and the tension terms have larger mean values as B_0 increases, and those for the stretching term remain almost same. Such a clear trend illustrates that the effect of magnetic fields on generation of solenoidal modes becomes stronger as B_0 increases.

Figure 20 shows average values of $\langle|\frac{1}{\rho^2}\nabla\rho\times\nabla P_B|\rangle$, $\langle|\nabla\times\frac{T}{\rho}|\rangle$, and $\langle|(\boldsymbol{w}\cdot\nabla)\boldsymbol{v}|\rangle$ after saturation, which are denoted by circles, "X" markers, and triangles, respectively, as a function of B^2. The gray shaded region shows 1σ dispersion about the average value of $\langle|(\boldsymbol{w}\cdot\nabla)\boldsymbol{v}|\rangle$ for the HD simulation, Run F512MS1-Hydro. The inset in the upper left corner is a zoom-in to clearly show the trend of $\langle|\frac{1}{\rho^2}\nabla\rho\times\nabla P_B|\rangle$ and $\langle|(\boldsymbol{w}\cdot\nabla)\boldsymbol{v}|\rangle$ with B^2.

The figure shows that the magnetic tension term is largest—and the inset shows that the magnetic pressure term is smallest—for all values of B^2. As in Figure 17, the magnetic tension term is roughly proportional to B^2. Note that its dependence on B^2 is very steep and it becomes much larger than others when $B^2 \gtrsim 0.1$. This implies that, as B^2 increases, the tension of magnetic field lines becomes more important and Alfvenization of compressively driven turbulence occurs. As a consequence, when B_0 is large (i.e., B^2 is large), compressively driven turbulence yields a significant amount of the solenoidal velocity component via the efficient role of the magnetic tension.

So far, we have discussed why large B_0 results in substantial solenoidal modes in turbulence driven by compressive driving. We have found that the effect of magnetic tension is most important. To clearly demonstrate this, we present (Figure 21) power spectra of $\boldsymbol{v}_{\rm sol}$ for $t_{\rm code}/t_{\rm ed} \leqslant 1$. The upper panels of Figure 21 show the time evolution of both $\langle v_{\rm sol}^2\rangle$ (red curves) and $\langle v_{\rm comp}^2\rangle$ (blue curves), and the lower panels show the power spectra of $\boldsymbol{v}_{\rm sol}$. The left, middle, and right panels correspond to Run F512MS1-Hydro, Run F512MS1-$B_0$0.01, and Run F512MS1-$B_0$0.6, respectively. The circles with different colors in the upper panels denote moments at which power spectra in the lower panels are calculated. The black curves in the lower panels are the power spectra after saturation.

We can immediately note the difference in the power spectra. If we compare sky-blue curves in the lower panels, the power spectra peak at different wavenumbers. The peak wavenumber

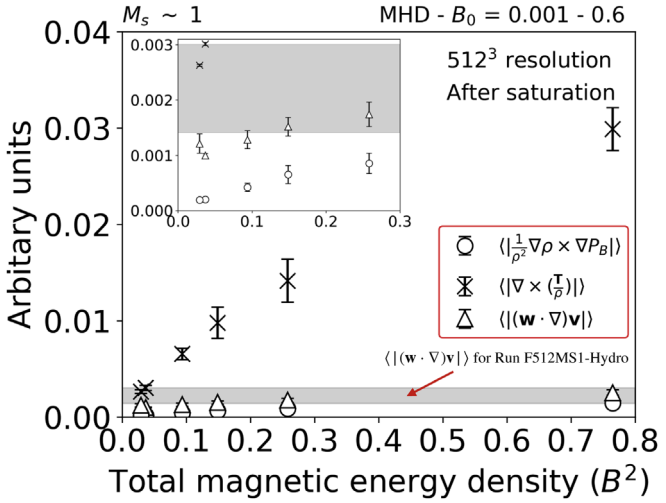

Figure 20. Average values of $\langle|\frac{1}{\rho^2}\nabla\rho\times\nabla P_B|\rangle$ (circles), $\langle|\nabla\times\frac{T}{\rho}|\rangle$ ("X" markers), and $\langle|(\boldsymbol{w}\cdot\nabla)\boldsymbol{v}|\rangle$ (triangles) at saturation as a function of total magnetic energy density (B^2). Gray shaded region represents 1σ dispersion about the average value of $\langle|(\boldsymbol{w}\cdot\nabla)\boldsymbol{v}|\rangle$ for the HD simulation, Run F512MS1-Hydro. Error bars represent the standard deviations. Inset in the upper left corner shows a zoom-in to more clearly illustrate the trend of $\langle|\frac{1}{\rho^2}\nabla\rho\times\nabla P_B|\rangle$ and $\langle|(\boldsymbol{w}\cdot\nabla)\boldsymbol{v}|\rangle$ with B^2.

for the HD simulation (left panel) is $k \approx 80$, which is closer to the dissipation scale, and moves to smaller wavenumbers as times go on. For $B_0 = 0.6$ (right panel), the power spectrum (in sky-blue) peaks at $k \approx 2.5$, corresponding to the driving scale, and then goes up without changing the peak wavenumber. The weak magnetic field case (middle panel) is intermediate between the two extreme cases.

We interpret the result of Figure 21 as follows. In the absence of magnetic field, as in the case of Run F512MS1-Hydro (left panel of Figure 21), we can reduce Equation (6) to

$$\frac{\partial \boldsymbol{w}}{\partial t} \sim -\nabla\cdot(\boldsymbol{v}w) + (\boldsymbol{w}\cdot\nabla)\boldsymbol{v} + \nu(\nabla^2 w + \nabla\times\boldsymbol{G}). \quad (7)$$

Since the first term on the rhs is conservative advection of the vorticity, the only contributing terms to the vorticity generation are the stretching (the second on the rhs) and the viscous dissipation (the third on the rhs) terms. In our simulations, vorticity is zero at the beginning and the compressive driving does not produce any vorticity later. Therefore, the vorticity in compressively driven HD turbulence is initially generated by the viscous dissipation term—which is responsible for the peak near the dissipation scale—and then amplified by the stretching

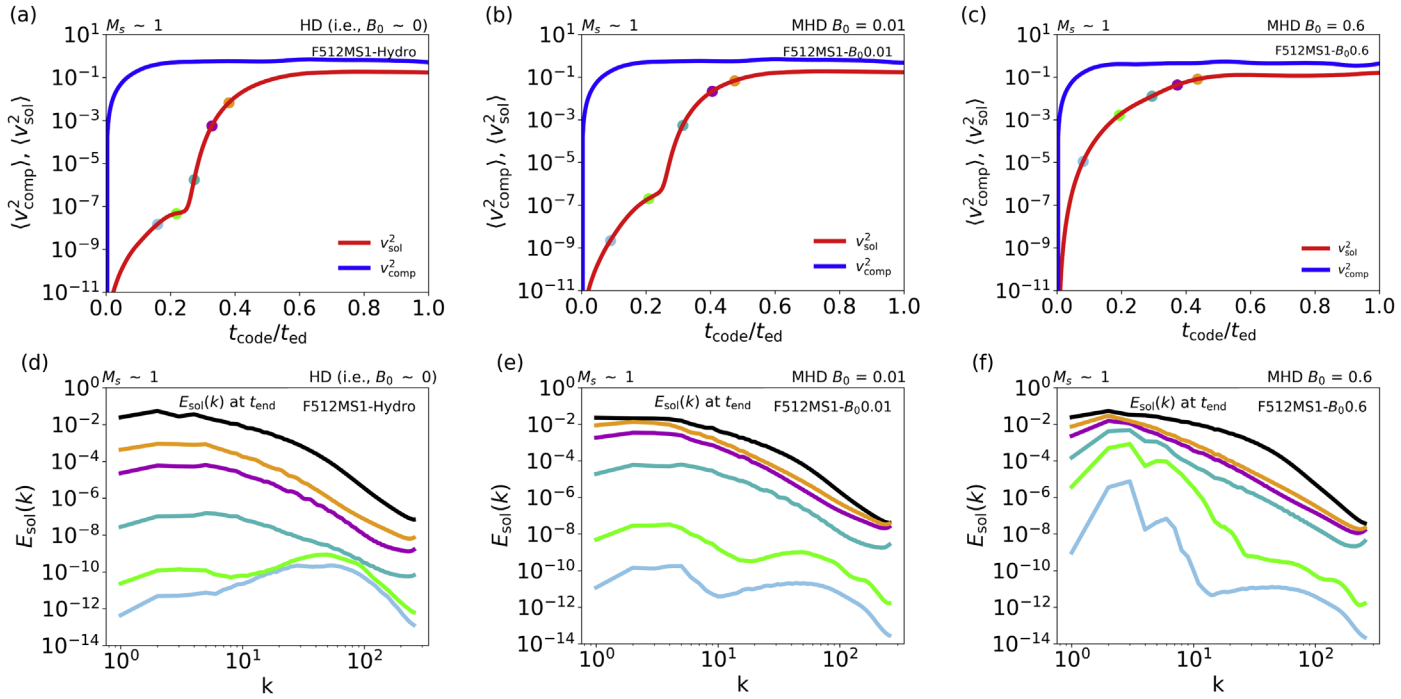

Figure 21. Time evolution of $\langle v_{comp}^2 \rangle$ and $\langle v_{sol}^2 \rangle$ (upper panels) and the power spectra of $\boldsymbol{v}_{sol}$ (lower panels) at the beginning of simulations. Left panels: Run F512MS1-Hydro. Middle panels: Run F512MS1-$B_0$0.01. Right panels: Run F512MS1-$B_0$0.6. Blue and red curves in the upper panels denote $\langle v_{comp}^2 \rangle$ and $\langle v_{sol}^2 \rangle$, respectively. Each colored circle in the upper panels denotes the moment at which the power spectrum with matching color in the lower panels is drawn. Black curves in the lower panels show power spectra after saturation.

effect (see also Mee & Brandenburg 2006; Federrath et al. 2011). As a consequence of the stretching effect, the peak position moves to smaller values of k as time goes on. On the other hand, when the mean magnetic field is initially strong, as in the case of Run F512MS1-$B_0$0.6 (right panel of Figure 21), the magnetic tension effect directly contributes to generating the solenoidal velocity component from the beginning, and thus the power spectrum can have a peak near the driving scale. When the mean magnetic field is initially weak, as in the case of Run F512MS1-$B_0$0.01 (middle panel of Figure 21), the process seems more complicated, and we suggest that the stretching and magnetic field effects play roles in conjunction because their strengths are comparable (see Figures 16(a) and (b)).

5.2. Effects of Correlation Timescale of Forcing Vectors

In Sections 3 and 4, we have found that the delta-correlated compressive driving results in lower solenoidal ratios and magnetic saturation levels than does the finite-correlated compressive driving with a similar M_s and the same numerical resolution. If a similar (in terms of direction and magnitude) driving is applied for a sufficiently long time, as in the case of the finite-correlated compressive driving, coherent generation of the solenoidal component occurs and the solenoidal velocity component can have a sufficiently long time to maintain its vortical motions once generated. We can more clearly illustrate this in terms of vorticity: if a coherent driving is applied for a long time, continued stretching of vorticity occurs until the forcing vector changes significantly, and as a result, stretching can be efficient. However, if a driving changes its amplitude and direction in a very short time interval, as in the case of the delta-correlated compressive driving, stretching of vorticity can be inefficient due to the frequent and abrupt change of the forcing vector. Therefore, it is understandable that the finite-correlated compressive driving generates a greater solenoidal velocity component. This argument is applicable to both HD and MHD turbulence.

In addition, the finite-correlated driving can generate a stronger small-scale magnetic field, which in turn helps turbulence driven by the finite-correlated driving to produce a greater solenoidal component in MHD turbulence. Similar to the stretching of vorticity, stretching of magnetic field lines can be more efficient in turbulence driven by the finite-correlated driving. Thus, the finite-correlated compressive driving can generate a stronger random magnetic field, which implies that the effect of magnetic field on the generation of solenoidal velocity component is more significant in the finite-correlated compressive driving. Therefore, we can conclude that the finite-correlated compressive driving generates a greater solenoidal velocity component.

Timescale of forcing vectors can also affect generation of compressive modes in *solenoidally* driven turbulence. When compressive modes are generated in solenoidally driven turbulence, they will produce density fluctuations. If the timescale of forcing is sufficiently long, as in the finite-correlated solenoidal driving, there can be time for gas pressure to (partially) counteract generation of the density fluctuations, which will (partially) suppress generation of compressive modes. There will not be such a suppression in the delta-correlated solenoidal driving case. Therefore, we expect that the latter driving scheme produces more compressive modes. Figure 22 clearly demonstrates that this argument is valid for solenoidally driven turbulence. In the figure, magenta and black curves correspond to the delta-correlated and the finite-correlated solenoidal drivings, respectively. We only consider $M_s \sim 1$ and 256^3 resolution. Unlike the other figures presented

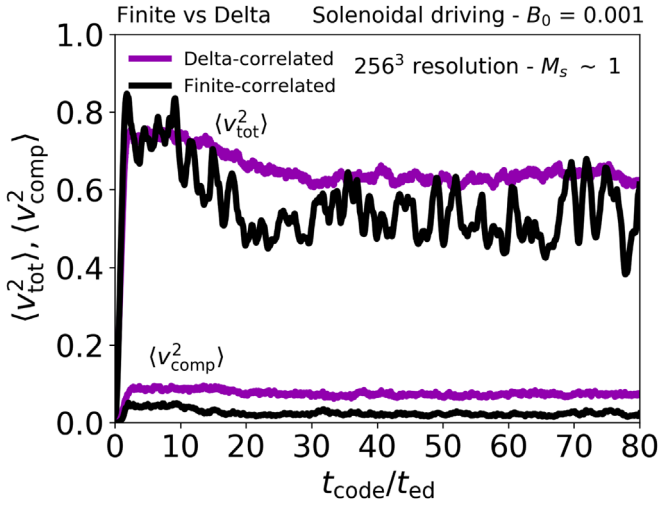

Figure 22. Time evolution of $\langle v_{tot}^2 \rangle$ and $\langle v_{comp}^2 \rangle$ for *solenoidally* driven turbulence with $B_0 = 0.001$ and $M_s \sim 1$. Magenta and black curves denote the delta-correlated and the finite-correlated solenoidal drivings, respectively. Note that we show $\langle v_{comp}^2 \rangle$, not $\langle v_{sol}^2 \rangle$, in this figure.

in Section 3, here we present the time evolution of $\langle v_{comp}^2 \rangle$. As can be seen, the delta-correlated solenoidal driving produces a higher level of $\langle v_{comp}^2 \rangle$ at saturation. This argument can also explain why the delta-correlated solenoidal driving has wider density PDFs (Yoon et al. 2016).

6. Discussion on Small-scale Turbulence Dynamo

As mentioned in Section 4.2, a small-scale turbulence dynamo in compressively driven turbulence is not significantly sensitive to numerical resolution. To compare this with a dynamo in solenoidally driven turbulence, we refer to Cho et al. (2009), who studied small-scale turbulence dynamos in incompressible turbulence driven by solenoidal driving.

Figure 23 shows the comparison. Blue and red circles indicate the magnetic saturation levels for 256^3 and 512^3 resolutions from our simulations, respectively. Black stars and black squares represent the magnetic saturation levels of the simulations with 64^3 and 96^3 resolutions from Cho et al. (2009), respectively.

First, we can see from Figure 23 that both solenoidally and compressively driven turbulence show a linear relation between B_0 and the magnetic saturation level. However, we note that the slopes are steeper for incompressible turbulence driven by the solenoidal driving. Second, the figure clearly shows an inefficient turbulence dynamo induced by the compressive driving: when $B_0 \lesssim 0.01$, the magnetic saturation levels from our 256^3 (blue circles) and 512^3 (red circles) resolution simulations are comparable to those from 64^3 resolution simulations of solenoidally driven incompressible turbulence (black stars). When $B_0 > 0.01$, even 64^3 resolution simulations of incompressible turbulence driven by the solenoidal driving show higher magnetic saturation levels than compressible turbulence with 512^3 resolution driven by the compressive driving. Third, for solenoidally driven turbulence, magnetic saturation level is very sensitive to numerical resolution (compare black squares with black stars), while it is not for compressively driven turbulence (compare red circles with blue ones). Therefore, the comparison suggests that a compressive driving would not effectively amplify small-scale magnetic fields, even though numerical resolution becomes very high.

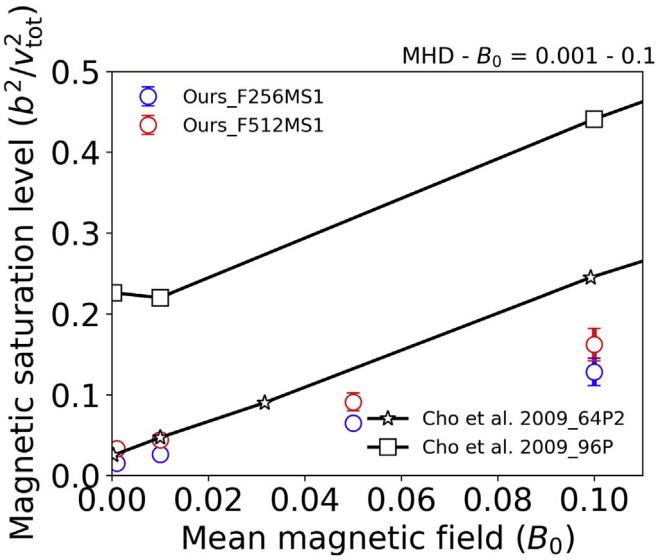

Figure 23. Comparison of the magnetic saturation level from our simulations for $M_s \sim 1$ with that from simulations of Cho et al. (2009), who used solenoidal driving and considered incompressible turbulence. Blue circles and red circles correspond to the results from our 256^3 and 512^3 resolution simulations, respectively. Black stars and black squares denote 64P2 and 96P simulation results from Cho et al. (2009), respectively. According to their notation, 64 or 96 refer to the number of grid points in each spatial direction, and P2 or P refer to physical viscosity.

Due to inefficiency of turbulence dynamos in compressively driven turbulence, it is very difficult to estimate the saturation level of magnetic energy density in the limit of a very high numerical resolution. However, we may at least conjecture with regard to the upper limit for the saturation level. In solenoidally driven turbulence with magnetic Prandtl number of ~ 1, the magnetic saturation level is slightly less than unity. Since solenoidal motions are mainly responsible for magnetic field growth, it is not plausible for magnetic energy to be greater than solenoidal energy. If this is true, we expect that the magnetic saturation level in the limit of a very high numerical resolution is less than 0.25 for $M_s \sim 1$, which is the solenoidal ratio for runs with no or a very small mean magnetic field. We will address this issue elsewhere.

7. Summary

In this paper, we have studied the generation of the solenoidal velocity component and small-scale magnetic field in compressively driven turbulence. In this regard, we have quantified the effects of the sonic Mach number (M_s) and the mean magnetic field (B_0). Moreover, we have considered two different driving schemes in terms of different correlation timescales of forcing vectors: a finite-correlated driving and a delta-correlated driving. Our main findings are as follows:

1. *The effect of the sonic Mach number (M_s) on the generation of the solenoidal velocity component.* We have shown that the higher M_s is, the greater the solenoidal velocity component generated in compressively driven turbulence, in both strong and weak mean magnetic field cases.
2. *The effect of mean magnetic field (B_0) on the generation of the solenoidal velocity component.* We have found that when B_0 is small, compressive driving yields a solenoidal velocity component similar to that from hydrodynamic

turbulence. However, when B_0 exceeds a certain value, it produces more of the solenoidal velocity component than hydrodynamic turbulence.

3. *The effect of M_s on the generation of small-scale magnetic field components.* We have examined that, when B_0 is small, the saturation level of the small-scale magnetic field component peaks at $M_s \sim 1$ for the finite-correlated compressive driving and shows monotonic increase when $M_s \lesssim 3$ for the delta-correlated compressive driving. When B_0 is very large, both driving schemes show similar behaviors: they produce a maximum saturation level at $M_s \sim 1$, and the level gradually decreases as M_s increases.
4. *The effect of B_0 on the generation of small-scale magnetic field components.* We have revealed that, as B_0 increases, more small-scale magnetic field components are generated in compressively driven turbulence. Moreover, the saturation level of the magnetic field follows an approximately linear relation with B_0 as in solenoidally driven turbulence.
5. *The effect of numerical resolution.* We have shown that generation of solenoidal velocity components is virtually independent of numerical resolution, and that of small-scale magnetic field is mildly sensitive to numerical resolution in compressively driven turbulence.
6. *The effect of a driving scheme*. When M_s is similar and the numerical resolution is the same, we have found that the finite-correlated driving always generates a greater solenoidal velocity component than does the delta-correlated driving. The trend is also observed in the case of solenoidally driven turbulence.

We have analyzed the vorticity equation to examine the effects of M_s and B_0 on the generation of a solenoidal velocity component provided by compressive driving:

1. For hydrodynamic turbulence, viscous dissipation initially generates vorticity, and then vortex stretching amplifies it.
2. For MHD turbulence with strong mean magnetic fields, magnetic tension is in effect; it directly produces solenoidal modes from the beginning, which is responsible for large amounts of solenoidal velocity component in cases of strong mean magnetic field. For weak mean magnetic field cases, vortex stretching and magnetic field play roles simultaneously.

In addition, we have discussed small-scale dynamos in compressively driven turbulence. We have compared a small-scale turbulence dynamo driven by compressive driving with that due to solenoidal driving from Cho et al. (2009). We have found that the magnetic saturation levels from our 256^3 and 512^3 resolution simulations are comparable to those from their 64^3 resolution simulations in a weak mean magnetic field regime, which implies inefficient dynamo action in compressively driven turbulence (Federrath et al. 2011). We have obtained that the solenoidal ratio is $\sim$0.25 for compressively driven turbulence with no or a very weak mean magnetic field. Since it is not plausible for magnetic energy to be larger than solenoidal energy, we may conjecture that the magnetic saturation level at an arbitrarily high numerical resolution is less than 0.25 for $M_s \sim 1$.

This paper has been expanded from a chapter of Jeonghoon Lim's Master thesis. This work is supported by the National R & D Program through the National Research Foundation of Korea Grants funded by the Korean Government (NRF-2016R1A5A1013277 and NRF-2016R1D1A1B02015014).

ORCID iDs

Jeonghoon Lim https://orcid.org/0000-0003-2719-6640
Jungyeon Cho https://orcid.org/0000-0003-1725-4376
Heesun Yoon https://orcid.org/0000-0003-4659-0758

References

Batchelor, G. K. 1950, RSPSA, 201, 405
Bertoglio, J.-P., Bataille, F., & Marion, J.-D. 2001, PhFl, 13, 290
Boldyrev, S., Nordlund, Å, & Padoan, P. 2002, ApJ, 573, 678
Brandenburg, A., & Subramanian, K. 2005, PhR, 417, 1
Brunetti, G., & Jones, T. W. 2014, IJMPD, 23, 1430007
Carilli, C. L., & Taylor, G. B. 2002, ARA&A, 40, 319
Cho, J. 2014, ApJ, 797, 133
Cho, J., & Lazarian, A. 2002, PhRvL, 88, 245001
Cho, J., & Lazarian, A. 2003, MNRAS, 345, 325
Cho, J., & Ryu, D. 2009, ApJL, 705, L90
Cho, J., & Vishniac, E. T. 2000, ApJ, 538, 217
Cho, J., Vishniac, E. T., Beresnyak, A., Lazarian, A., & Ryu, D. 2009, ApJ, 693, 1449
Cho, J., & Yoo, H. 2012, ApJ, 759, 91
Crutcher, R. M. 2012, ARA&A, 50, 29
Elmegreen, B. G., & Scalo, J. 2004, ARA&A, 42, 211
Federrath, C. 2013, MNRAS, 436, 1245
Federrath, C. 2016, JPlPh, 82, 535820601
Federrath, C., Chabrier, G., Schober, J., et al. 2011, PhRvL, 107, 114504
Federrath, C., & Klessen, R. S. 2012, ApJ, 761, 156
Federrath, C., Klessen, R. S., & Schmidt, W. 2008, ApJL, 688, L79
Federrath, C., Klessen, R. S., & Schmidt, W. 2009, ApJ, 692, 364
Federrath, C., Roman-Duval, J., Klessen, R. S., Schmidt, W., & Mac Low, M. M. 2010, A&A, 512, A81
Govoni, F., & Feretti, L. 2004, IJMPD, 13, 1549
Haugen, N. E. L., Brandenburg, A., & Dobler, W. 2003, ApJL, 597, L141
Haugen, N. E. L., Brandenburg, A., & Dobler, W. 2004, PhRvE, 70, 016308
Hennebelle, P., & Inutsuka, S.-i 2019, FrASS, 6, 5
Hitomi Collaboration, Aharonian, F., Akamatsu, H., et al. 2016, Natur, 535, 117
Kritsuk, A. G., Norman, M. L., Padoan, P., & Wagner, R. 2007, ApJ, 665, 416
Kritsuk, A. G., Ustyugov, S. D., Norman, M. L., & Padoan, P. 2010, in ASP Conf. Ser. 429, Numerical Modeling of Space Plasma Flows, ed. N. V. Pogorelov, E. Audit, & G. P. Zank (San Francisco, CA: ASP), 15
Krumholz, M. R., & Federrath, C. 2019, FrASS, 6, 7
Kulsrud, R. M., Cen, R., Ostriker, J. P., & Ryu, D. 1997, ApJ, 480, 481
Larson, R. B. 1981, MNRAS, 194, 809
Mac Low, M.-M., & Klessen, R. S. 2004, RvMP, 76, 125
McKee, C. F., & Ostriker, E. C. 2007, ARA&A, 45, 565
Mee, A. J., & Brandenburg, A. 2006, MNRAS, 370, 415
Porter, D. H., Jones, T. W., & Ryu, D. 2015, ApJ, 810, 93
Ryu, D., Kang, H., Cho, J., & Das, S. 2008, Sci, 320, 909
Ryu, D., Schleicher, D. R. G., Treumann, R. A., Tsagas, C. G., & Widrow, L. M. 2012, SSRv, 166, 1
Schekochihin, A. A., Cowley, S. C., Taylor, S. F., Maron, J. L., & McWilliams, J. C. 2004, ApJ, 612, 276
Schekochihin, A. A., Iskakov, A. B., Cowley, S. C., et al. 2007, NJPh, 9, 300
Schuecker, P., Finoguenov, A., Miniati, F., Böhringer, H., & Briel, U. G. 2004, A&A, 426, 387
Vazza, F., Jones, T. W., Brüggen, M., et al. 2017, MNRAS, 464, 210
Yoon, H., & Cho, J. 2019, ApJ, 880, 137
Yoon, H., Cho, J., & Kim, J. 2016, ApJ, 831, 85